Article

Early Detection and Staging of Lung Fibrosis Enabled by Collagen-Targeted MRI Protein Contrast Agent

Oluwatosin Y. Ibhagui, Dongjun Li, Hongwei Han, Guangda Peng, Maureen L. Meister, Zongxiang Gui, Jingjuan Qiao, Mani Salarian, Bin Dong, Yi Yuan, Yiting Xu, Hua Yang, Shanshan Tan, Ganesh Satyanarayana, Shenghui Xue, Ravi Chakra Turaga, Malvika Sharma, Yan Hai, Yuguang Meng, Khan Hekmatyar, Phillip Sun, Gabriel Sica, Xiangming Ji, Zhi-ren Liu, and Jenny J. Yang*
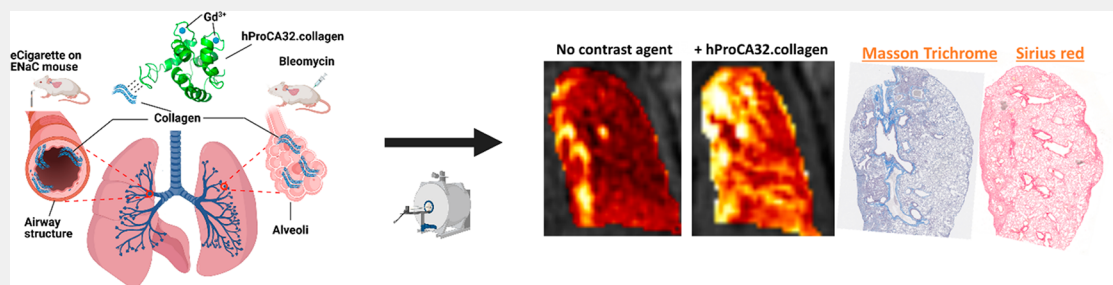
Cite This: *Chem. Biomed. Imaging* 2023, 1, 268−285

Read Online

ACCESS | Metrics & More | Article Recommendations | SI Supporting Information

ABSTRACT: Chronic lung diseases, such as idiopathic pulmonary fibrosis (IPF) and chronic obstructive pulmonary disease (COPD), are major leading causes of death worldwide and are generally associated with poor prognoses. The heterogeneous distribution of collagen, mainly type I collagen associated with excessive collagen deposition, plays a pivotal role in the progressive remodeling of the lung parenchyma to chronic exertional dyspnea for both IPF and COPD. To address the pressing need for noninvasive early diagnosis and drug treatment monitoring of pulmonary fibrosis, we report the development of human collagen-targeted protein MRI contrast agent (hProCA32.collagen) to specifically bind to collagen I overexpressed in multiple lung diseases. When compared to clinically approved Gd^{3+} contrast agents, hProCA32.collagen exhibits significantly better r_1 and r_2 relaxivity values, strong metal binding affinity and selectivity, and transmetalation resistance. Here, we report the robust detection of early and late-stage lung fibrosis with stage-dependent MRI signal-to-noise ratio (SNR) increase, with good sensitivity and specificity, using a progressive bleomycin-induced IPF mouse model. Spatial heterogeneous mapping of usual interstitial pneumonia (UIP) patterns with key features closely mimicking human IPF, including cystic clustering, honeycombing, and traction bronchiectasis, were noninvasively detected by multiple MR imaging techniques and verified by histological correlation. We further report the detection of fibrosis in the lung airway of an electronic cigarette-induced COPD mouse model, using hProCA32.collagen-enabled precision MRI (pMRI), and validated by histological analysis. The developed hProCA32.collagen is expected to have strong translational potential for the noninvasive detection and staging of lung diseases, and facilitating effective treatment to halt further chronic lung disease progression.

KEYWORDS: IPF, COPD, MRI, fibrosis, heterogeneity, early detection, lung disease, collagen

1. INTRODUCTION

According to the World Health Organization (WHO), chronic lung diseases, including idiopathic pulmonary fibrosis (IPF) and chronic obstructive pulmonary disease (COPD), are common respiratory conditions that are significant public health burdens. IPF and COPD are major leading causes of death that currently affect over 300 million patients worldwide.[1] IPF from unknown etiologies is the most common and deleterious of interstitial lung diseases with a very poor prognosis, accounting for about 40,000 deaths per year in the U.S. alone,[2] while COPD, commonly caused by cigarette smoking, is the third leading cause of death globally. Health
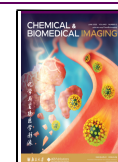
officials have become increasingly concerned that vapor from electronic cigarettes can increase the risk of lung diseases, including lung fibrosis, although the mechanism is not yet fully understood.[3] Both IPF and E-cigarette-induced fibrosis in COPD are characterized by progressive remodeling of the lung
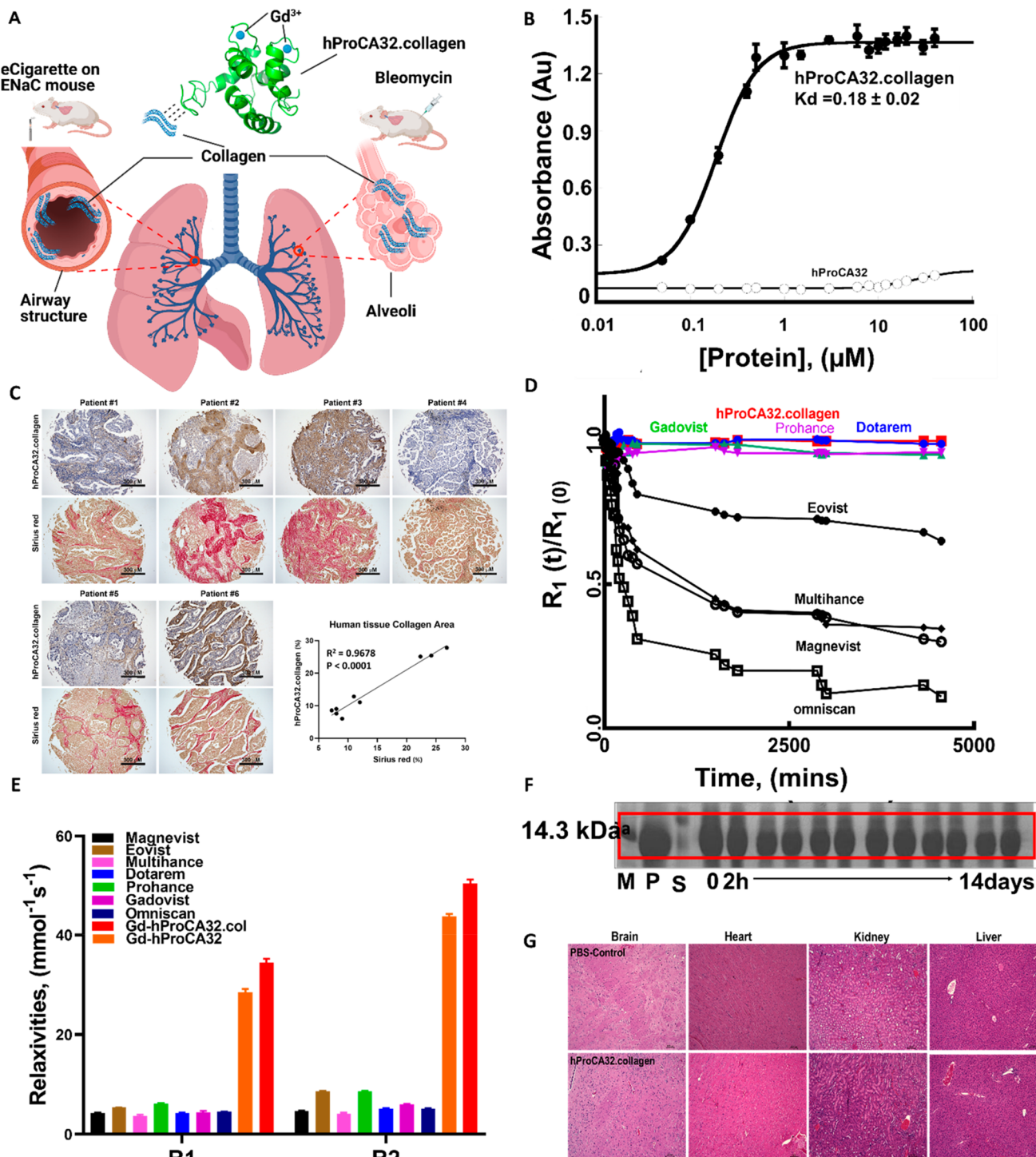
Figure 1. Design and characterization of hProCA32.collagen for lung fibrosis detection. (A) Collagen accumulation and binding in bleomycin-induced IPF (right) and airway fibrosis (left) with overexpression of collagen (blue color) at the alveolar and the bronchial airways, respectively. (B) Estimation of the collagen-binding affinity of hProCA32.collagen to collagen type I using modified indirect ELISA assay. No collagen I binding was observed for hProCA32 (PEGylated, non-targeted agent). (C) hProCA32.collagen (brown color) exhibits strong specificity to overexpressed collagen I in human patient tissue as evidenced by the similarities in pattern and collagen content compared to Sirius Red (red color) stained human tissue ($R^2 = 0.97$, $P < 0.0001$); all scale bars, 300 μm. (D) Changes in relaxation rates (transmetalation susceptibility) of hProCA32.collagen compared to those of clinical contrast agents in the presence of $ZnCl_2$ at different time points up to 4 days. (E) Relaxivity r_1 and r_2 values of PEGylated nontargeted hProCA32 and hProCA32.collagen (hProca32.col) at clinical field strength (1.4 T), 37 °C, compared to those of commercial clinical contrast agents. (F) Serum stability test of hProCA32.collagen shows that hProCA32.collagen remained intact in serum for up to 14 days (M, protein marker; P, hProCA32.collagen only; S, serum only). (G) Representative H&E histological tissue sections of hProCA32.collagen-injected mice exhibit no tissue cytotoxicity, as was also observed with PBS-injected mice (n = 3 per group).

Table 1. Comparison of Stability Constants of Commercially Available Gadolinium-Based Contrast Agents with hProCA32, hProCA32.collagen, and rProCA32.collagen1 at 25 °C

contrast agent	log (K_{Tb})	injection dosage (mmol/kg)	log (K_{Gd})	log (K_{Ca})	log (K_{Zn})	log (K_{Gd}/K_{Ca})	log (K_{Gd}/K_{Zn})
Magnevist[a]	22.00	0.1	22.46	10.75	18.60	12.24	4.13
ProHance[a]	N/A[c]	0.1−0.3	23.80	14.83	19.37	10.07	4.37
Eovist[a]	N/A[c]	0.025	23.60	11.82	18.78	12.22	5.18
Dotarem[a]	N/A[c]	0.1	24.70	16.37	18.70	7.46	3.65
MultiHance[a]	N/A[c]	0.05	22.59	N/A[c]	17.04	N/A[c]	4.87
Omniscan	N/A[c]	0.1	16.85	7.17	12.04	9.68	4.81
Gadovist	N/A[c]	0.1	N/A[b]	N/A[c]	N/A[c]	N/A[c]	N/A[c]
hProCA32[b]	22.53[c]	0.0013	22.54[b]	8.71[b]	6.36[b]	14.7	16.2
rProCA32.collagen1[b]	**22.80**	**0.0013**	**22.30**[b]	**8.70**[b]	**6.12**[b]	**14.4**	**16.2**
hProCA32.collagen[b]	**22.03**	**0.0013**	**22.2**[b]	**8.11**[b]	**6.8**[b]	**14.1**	**15.4**

[a]Stability constants of clinical contrast agents measured by pH potentiometric method.[19] [b]Stability constants measured by the fluorescence resonance transfer between tryptophan and metal in protein contrast agents.[20] [c]N/A: Not available.

parenchyma to chronic exertional dyspnea with increased heterogeneous extracellular matrix (ECM) deposition, including collagen type I.[4,5] In addition, recent studies have shown that >30% of patients with infectious diseases such as severe acute respiratory syndrome coronavirus 2 (SARS-CoV-2) presented fibrotic-like changes in the lung. This sharp increase in lung injuries and death has created an imperative and pressing need for noninvasive early detection and staging of chronic and acute lung disease by quantifying molecular biomarker expression as well as for preclinical application for drug discovery.

To date, there are no noninvasive and quantitative diagnostic tools with sufficient sensitivity to detect early-stage lung fibrosis during disease progression and to monitor treatment response. The current gold standard for IPF diagnosis involves high-resolution computed tomography (HRCT), which categorizes lung abnormalities into usual interstitial pneumonia (UIP) patterns, probable UIP patterns, indeterminate for UIP patterns, and alternative diagnosis.[6] The most important requirement for a definitive diagnosis of IPF in HRCT is the presence of apicobasal honeycombing, subpleural lower lobe reticular opacities, or traction bronchiectasis. However, these radiologic hallmarks of IPF are missed by HRCT in at least 30% of patients who were later diagnosed with IPF by surgical lung biopsy and related histopathological findings.[7,8] Thus, additional invasive surgical lung biopsy is still required for further diagnosis. Unfortunately, surgical lung biopsy in patients with suspected IPF often has high sampling error and high risk associated with comorbidities.[9,10]

To address the pressing need for noninvasive early diagnosis and monitoring of drug treatment for pulmonary fibrosis, here, we report the development of human collagen-targeted protein MRI contrast agent (hProCA32.collagen) to specifically bind to collagen I overexpressed in multiple lung diseases. Compared to clinically approved Gd^{3+} contrast agents, hProCA32.collagen exhibits greatly improved r_1 and r_2 relaxivity, strong metal binding affinity and selectivity, and better transmetalation resistance. We further report the robust detection of early- and late-stage lung fibrosis with stage-dependent MRI signal-to-noise ratio (SNR) increase, with good sensitivity and specificity, using a newly established progressive bleomycin-induced IPF mouse model and nicotine-induced COPD mouse model. The hProCA32.collagen contrast agent is expected to have strong translational potential for noninvasive detection and staging of lung diseases

and facilitating effective treatment to halt further chronic lung disease progression.

2. RESULTS

2.1. Developed Collagen-Targeted Contrast Agent hProCA32.collagen Exhibits High Relaxivity, Metal Binding Affinity, and Collagen Binding Capability

Figure 1A illustrates the designed collagen-targeted MRI contrast agent, hProCA32.collagen, which contains a collagen type I targeting peptide moiety flanked with a flexible hinge connected to the C-terminal of the protein contrast agent, hProCA32 (with two Gd^{3+} binding sites) in human α-parvalbumin. hProCA32.collagen is different from previously reported ProCA32.collagen1 (hereafter denoted as rProCA32.-collagen1) constructed with rat protein parvalbumin, which differs from the human protein by 9 amino acid residues in nonmetal binding regions.[11−13] After bacterial expression and purification, the designed protein was PEGylated at lysine residues and formulated as a 2:1 Gd^{3+}-hProCA32.collagen complex, verified by mass spectrometry and SDS-PAGE[12,14] (Figure S1).

hProCA32.collagen exhibits strong binding affinity to type I collagen, with a K_d of 0.18 ± 0.02 μM (Figure 1B), which is sensitive to the pathological concentration of overexpressed collagen I (∼1−20 μM).[15−17] Its binding affinity for type I collagen is 6.3- and 13-fold stronger than for collagen types III and IV (Figure S2), respectively. In contrast, hProCA32, without the targeting moiety, lacks the ability to bind to collagen I. To evaluate the translational capability of hProCA32.collagen, we assessed the binding and specificity of hProCA32.collagen to human collagens in vitro (Figure S2) and in the lung using human lung tissue microarray (US Biomax, inc. catalog #LC 561), and compared the results against collagen-specific Sirius Red staining (Figure 1C; top row and bottom row, respectively). Immunostaining analysis demonstrated that hProCA32.collagen binds to human collagen in patient lung fibrosis tissue samples with a collagen pathological pattern similar to that observed with Sirius Red staining. Quantification of collagen area per slice in all stained microarrays exhibited a linear correlation ($R^2 = 0.97$, $P < 0.0001$) between hProCA32.collagen and Sirius Red (Figure 1C).

Transmetalation studies (Figure 1D) demonstrated that the Gd^{3+}−hProCA32.collagen complex has stability comparable to that of macrocyclic contrast agents Gadovist, Dotarem, and
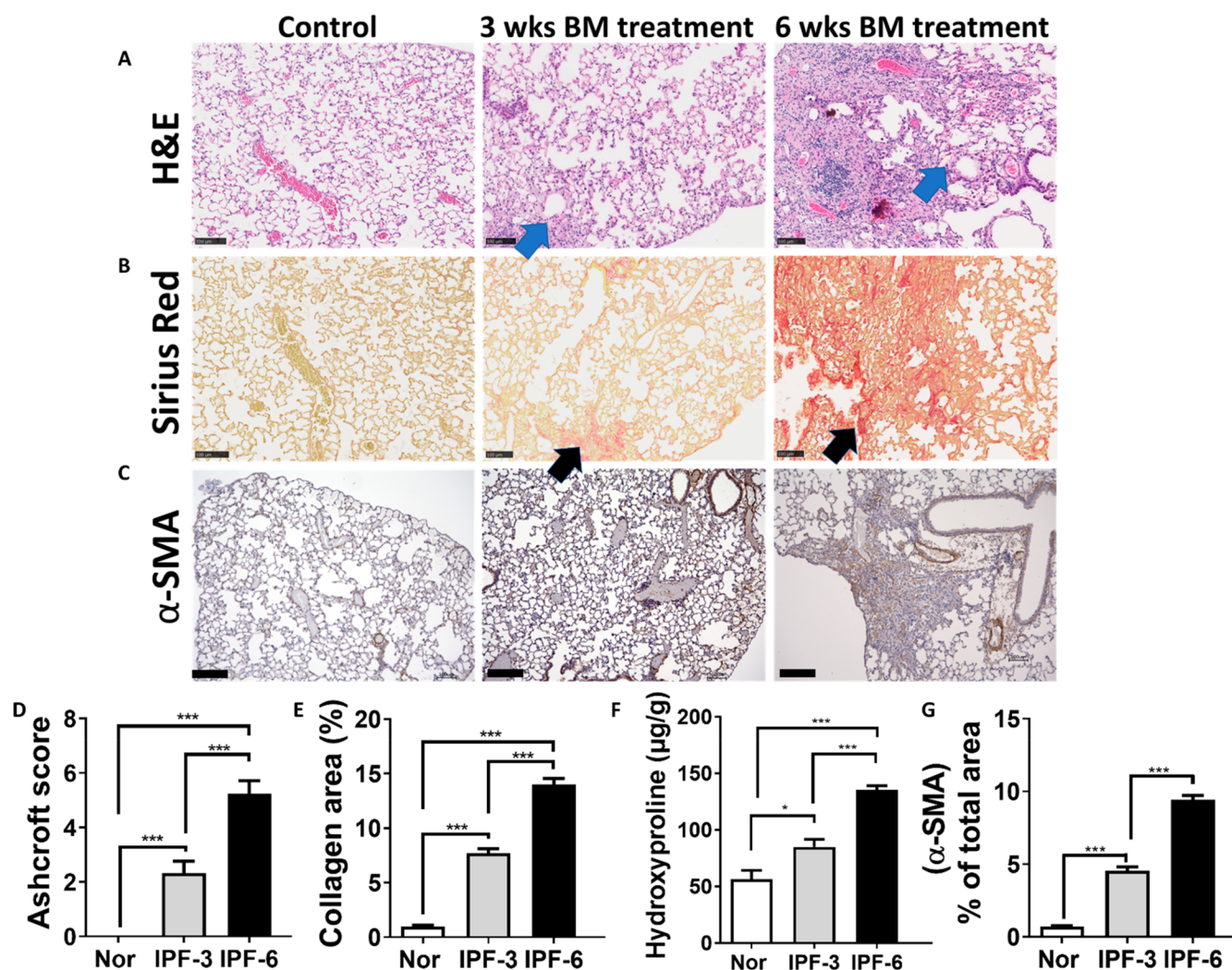
Figure 2. Characterization of bleomycin-induced IPF mouse model. (A) Representative images of bleomycin-induced mouse stained with hematoxylin and eosin (H&E) with cystic honeycombing features (arrow). (B) Sirius Red with red area indicative of collagen deposition (black arrow). (C) α-Smooth muscle actin (α-SMA). (D) Ashcroft scoring of normal, early-, and late-stage bleomycin-induced mice. (E−G) Quantification of collagen area, hydroxyproline, and α-SMA in normal and bleomycin-induced IPF mouse models. Scale bar for all images = 100 μm. All data are shown as mean ± SD, n = 4 per group, ***P < 0.0001, *P < 0.05 Student's t test.

ProHance against physiological metal ion zinc. In contrast, linear contrast agents such as Omniscan, Eovist, and MultiHance, are much less stable against transmetalation. hProCA32.collagen exhibits 8- to 10-fold improvement in both r_1 and r_2 compared to current clinically used contrast agents such as Dotarem and Gadovist, at both 1.4 and 7.0 T (Figures 1E and S3), with values of r_1 (32.0 ± 0.3 mM^{-1}·s^{-1}) and r_2 (51.0 ± 0.2 mM^{-1}·s^{-1}) per Gd^{3+} at 1.4 T, and r_1 (18.5 ± 1.5 mM^{-1}·s^{-1}) and r_2 (105.6 ± 2.0 mM^{-1}·s^{-1}) at 7.0 T, at 37 °C.[18,19] Because mice are ~1000-fold smaller than humans, high magnetic field strength is used to increase resolution. High r_1 and r_2 values of hProCA32.collagen at both low and high magnetic field strengths are important for translational studies for small animals. Additionally, hProCA32.collagen remains intact in serum for at least 14 days (Figure 1F) with no increase in the blood marker analysis and no tissue cytotoxicity and with no appreciable difference observed in H&E histological slides of mice injected with hProCA32.collagen versus PBS control mice (Figures 1G and S8). Further, hProCA32.collagen exhibits strong metal binding affinity and metal selectivity. The Gd^{3+} binding constant for hProCA32.-

collagen is comparable to that of DTPA and exhibits ~10^{11}-fold metal selectivity for Gd^{3+} over physiological metal ions such as Zn^{2+} with DTPA (Figure S4 and Table 1).

2.2. hProCA32.collagen-Enabled Dual MR Imaging Detection of Early- and Late-Stage IPF in Bleomycin-Induced Mice Model

The hProCA32.collagen-enabled MRI detection capability of lung fibrosis induced by intraperitoneal (I.P.) injection of bleomycin sulfate was evaluated at both early and late stages (3 and 6 weeks bleomycin (BM)-treated mice, respectively). Lung fibrosis development and progression in this mouse model displayed UIP patterns characterized and verified by H&E staining, ECM deposition measured by Sirius Red staining, hydroxyproline assay, and multiple fibrosis biomarker changes, including myofibroblasts and M2 macrophages indicated by α-SMA and arginase-I staining (Figures 2A−G and S5 and S6). The developed mouse model displays the two key features of fibrosis: dense parenchymal scar alternating with normal parenchyma and temporal lung heterogeneity. Collagen deposition (red) from Sirius stain was noticeably present with high density in late-stage IPF compared to the early stage
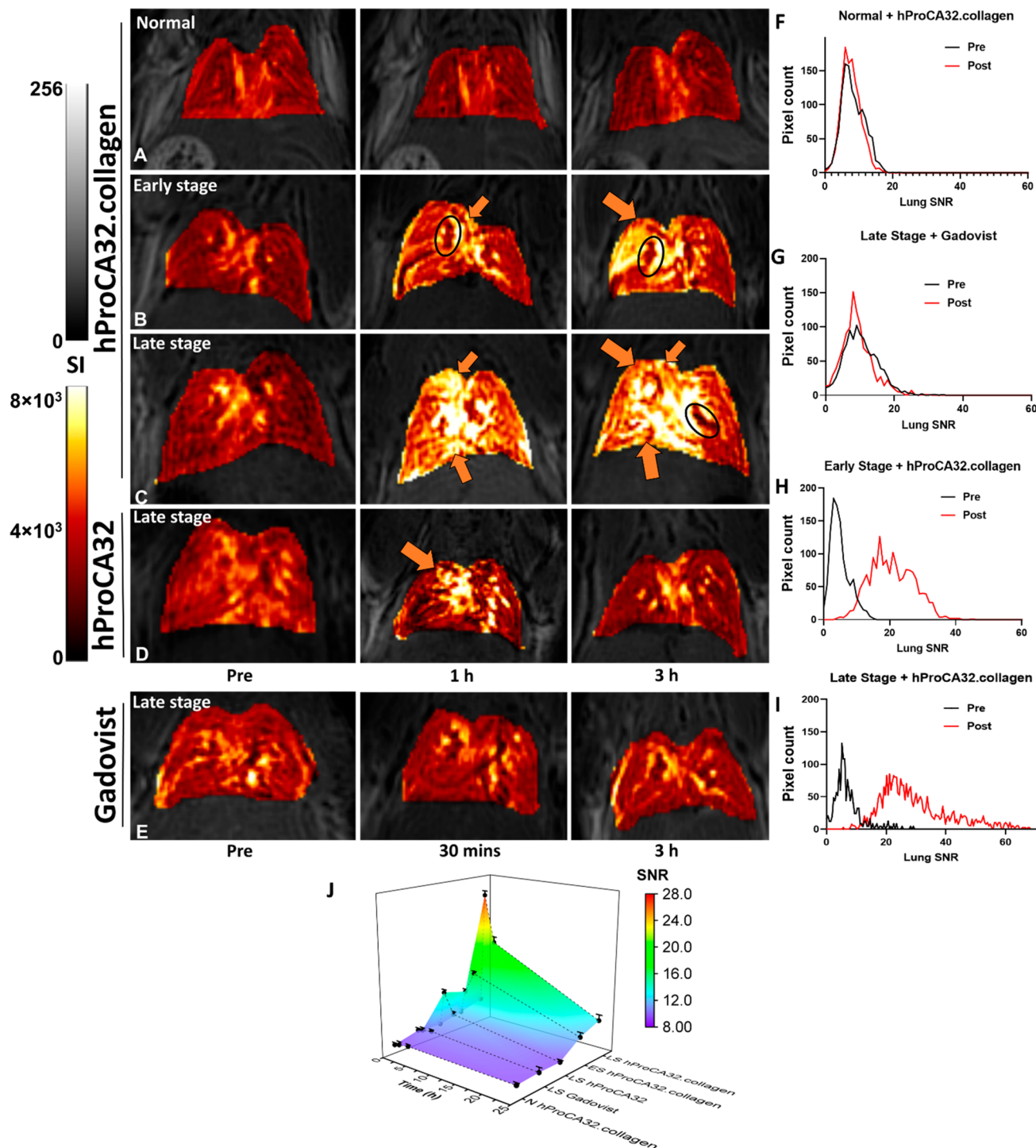
Figure 3. Detection of early (3 weeks post-BM treatment) and late-stage (6 weeks post-BM treatment) IPF at 7 T. Coronal view (with "false" color overlay) of T_1-weighted ultrashort echo time (UTE)-MRI of the lungs of normal (A), early-stage (B), and late-stage (C) BM-treated mice before (pre-injection), and then 1 h, and 3 h after injection of hProCA32.collagen; hProCA32.collagen-enabled detection of heterogeneous enhancement of collagenous honeycombing at the subpleural and paraseptal areas of the lung at early stage (B) and late stage (C), highlighted by orange arrows, and traction bronchiectasis highlighted with black circles. MR image changes were not observed in late-stage IPF mice at pre-, 1 h, and 3 h after injection of nontargeted hProCA32 (D) and at pre-, 30 min, and 3 h after injection of Gadovist (E). (F−I) Histogram pixel analysis of normal mice before and 1 h after injection of hProCA32.collagen (F), late-stage IPF mice before and 30 min after injection of Gadovist (G). Early-stage (H) and late-stage (I) mice before and 3 h after injection of hProCA32.collagen. (J) 3D SNR plot of entire MRI slices array before and after injection of hProCA32.collagen, Gadovist, and nontargeted hProCA32 in healthy, early-, and late-stage BM-induced IPF mouse models (LS, late stage; ES, early stage; N, normal; MR image color scales represent signal intensities).

with fibrosis, observed at the perilobular area of the lung. Furthermore, destruction of lung alveolar architecture, cystic honeycombing, and fibroblast foci were observed (Figures 2A−C and S5). The Ashcroft score[21] increased from 0 for normal mice to 2.3 ± 0.4 for 3 weeks post-BM-treated mice and 4.7 ± 1.2 for 6 weeks post-BM-treated mice (Figure 2D).
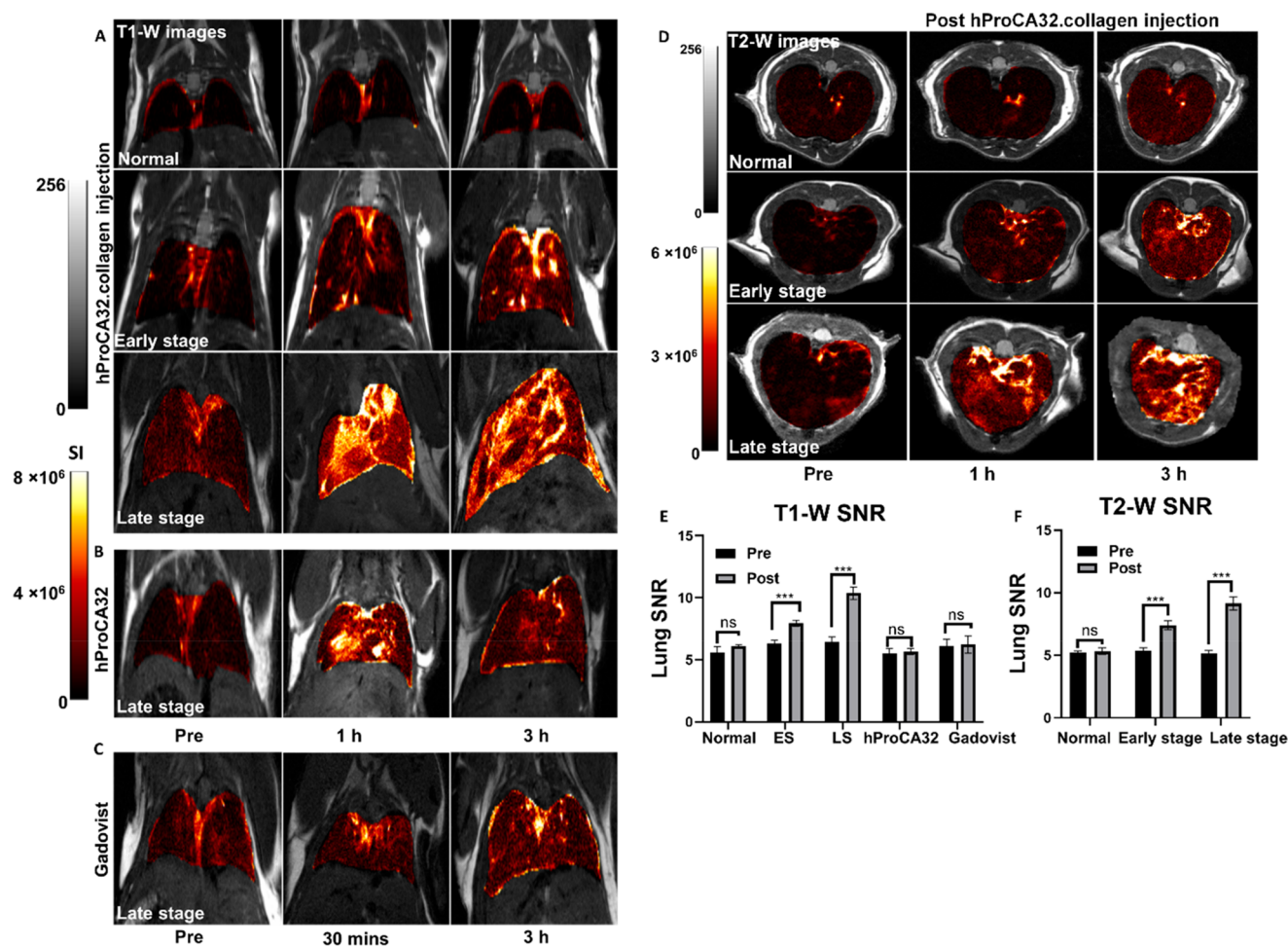
Figure 4. Dual lung imaging capability of hProCA32.collagen in IPF mice at 7 T. (A) Coronal T_1-W MR images (with "false" color overlay) of healthy mice, early- and late-stage mice before, 1 h, and 3 h after injection of hProCA32.collagen. (B) Coronal T_1-W MR images of late-stage mice before, 1 h, and 3 h post-injection of nontargeted hProCA32. (C) Coronal T_1-W MR images of late-stage mice before, 1 h, and 3 h post-injection of clinical contrast agent, Gadovist. (D) Axial T_2-W MR images (with "false" color overlay) of healthy, early-, and late-stage mice before, 1 h, and 3 h after injection of hProCA32.collagen. (E) T_1-W SNR plot of hProCA32.collagen-injected healthy (normal), early-stage (ES), late-stage (LS), nontargeted hProCA32-injected, and Gadovist-injected late-stage IPF mice. Significant increases were observed for ProCA32.collagen, while no appreciable increase was observed for late-stage IPF mice injected with either hProCA32 and Gadovist. (F) T_2-W SNR plot pre- and post- (3 h) injection of hProCA32.collagen of healthy mice and IPF mice at early and late stage showed a significant increase in lung SNR. All data are shown as mean ± SD, n = 4 biologically independent animals in each group, ***P < 0.001, ns = not significant, Student's t test. MR image color scales represent signal intensities.

The collagen area increased progressively at different stages from 1.0 ± 0.1% for normal mice, to 8.9 ± 0.2% for 3 weeks post-BM-treated mice, and to 13.2 ± 1.0% for 6 weeks post-BM-treated mice (Figure 2E). The hydroxyproline quantification reflected a progressive increase with disease advancement from 56.4 ± 13.6 μg/lung for normal mice, to 88.6 ± 12.6 μg/lung for 3 weeks post-BM-treated mice, and to 125.0 ± 17.4 μg/lung for 6 weeks post-BM-treated mice (Figure 2F). The α-SMA levels also increased with disease progression from 0.5 ± 0.2% in normal mice to 4.2 ± 0.1% for 3 weeks post-BM-treated mice and to 8.5 ± 0.4% for 6 week BM-treated mice (Figure 2G).

The imaging capability of hProCA32.collagen for both early- and late-stage IPF in the developed mouse model was examined. Both respiratory-gated T_1-weighted 3D ultrashort echo time (3D-UTE) with radial sampling (Figure 3A−E), and T_1-W rapid acquisition refocused echo (RARE) MRI and T_2-W fast spin echo RARE, before and after injection of contrast agents, were performed (Figure 4). In addition, Gadovist and

nontargeted hProCA32 in healthy and bleomycin-induced lung fibrotic mice were also compared. Injection of hProCA32.collagen contrast agent resulted in 60 and 80.5% enhancement at 3 h time point compared with pre-injection for the early and late stage of IPF mice, respectively, while injection of hProCA32.collagen into healthy normal mice did not result in any noticeable MRI enhancement (Figure 3A−C). Pixel analysis of the MRI images further supported the stage-dependent enhancement of the MRI signal enabled by hProCA32.collagen (Figure 3F−I) with greater differences in enhancement distribution for late-stage IPF mice. In contrast, injection of Gadovist and nontargeted hProCA32 into late-stage IPF mice did not result in either significant enhancement or distribution changes in pixel analysis of the images (Figure 3D,E,G). These changes in SNR were plotted as a 3D plot comparing SNR for all contrast agents (Figure 3J).

Next, we demonstrated that hProCA32.collagen could detect fibrotic networks in both early and late stages of IPF models using both T_1 and T_2 imaging with conventional MRI
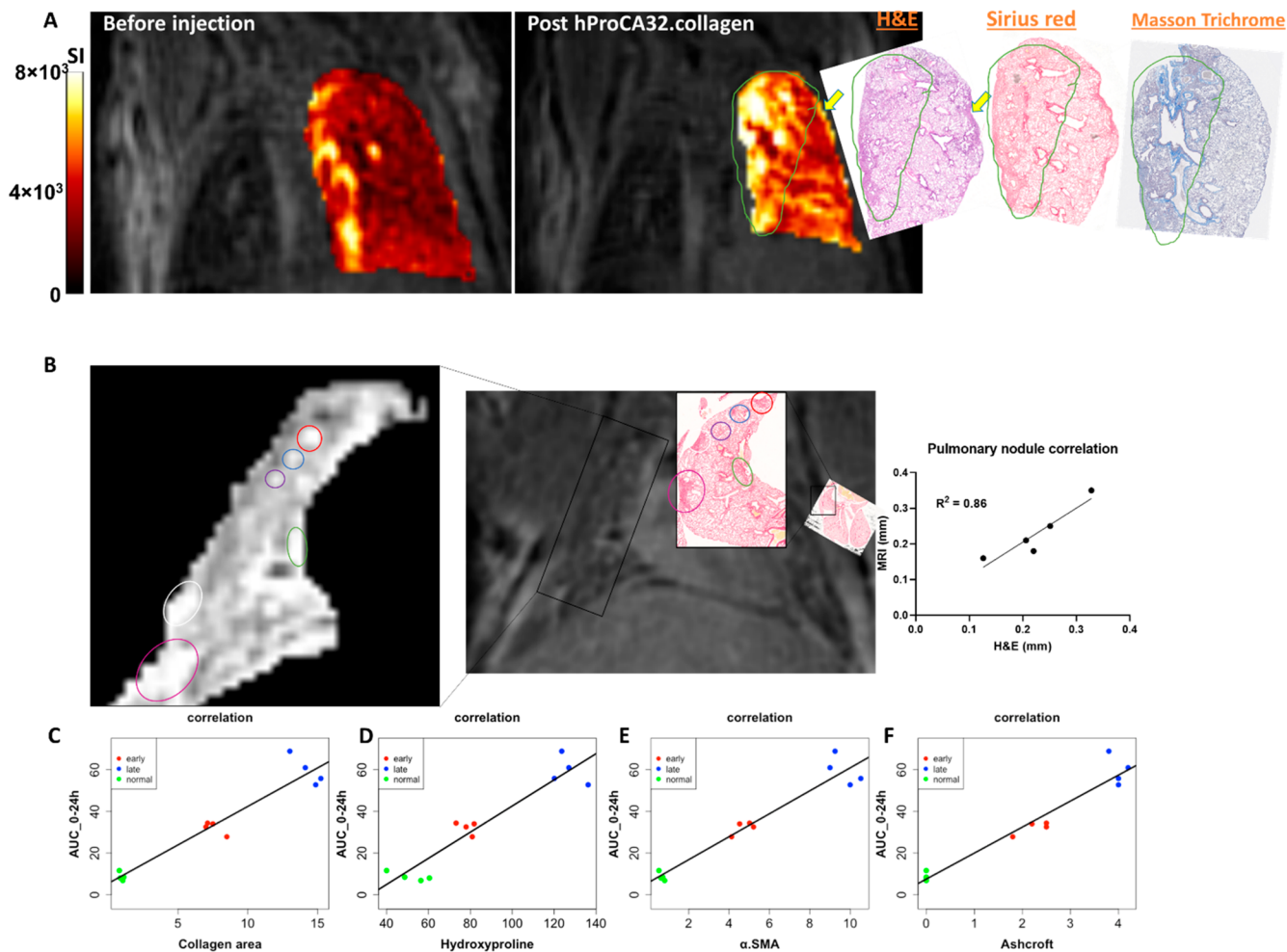
Figure 5. Correlation of hProCA32.collagen uptake in MRI with histological findings. (A) Representative coronal images of late-stage IPF mice before and 3 h after injection of hProCA32.collagen showed specific accumulation in areas with fibrosis (left image) compared to the pre-injection time point. This observed MRI enhancement closely resembled histological findings by H&E, Sirius Red, and Masson Trichrome staining. (B) Detection and correlation of specific MRI enhancements such as pulmonary nodules and observed fibrotic patch with Sirius Red collagen staining exhibited a linear correlation between MRI-detected pulmonary nodules and H&E. (C−F) Scatter plots of Logit-transformed collagen area, hydroxyproline level, α-SMA, and Ashcroft score, respectively, against area under the curve (AUC) AUC_0−24, revealed a linearly correlated histological quantification with MRI observation ($R^2 = 0.86$; MR image color scales represent signal intensities).

pulse sequences (RARE, FSEMS, and SEMS) (Figure 4). Injection of hProCA32.collagen resulted in 40 and 120% changes in lung SNR for early and late stages of IPF models, respectively, using T_1-W MRI. It also resulted in 25.2 and 61.5% increases in early- and late-stage IPF SNR values, respectively, in T_2-W MR images (obtained in axial orientation only). These significant changes and lung enhancements were absent in both normal mice and IPF mice injected with Gadovist.

As validated by histological analysis and histological and radiographic correlation (Figure 5), the detected MRI SNR enhancements using various imaging pulse sequences (Figures 3 and 4) are stage-dependent and strongly correlate to histological markers such as collagen content, hydroxyproline, and α-SMA content (Figure 5C−F).

MRI enhancement corresponds to collagen accumulation, as seen in Figure 3 and Figure 5A. In Figure 3, collagen located in the subpleural region (orange arrows) and traction bronchiectasis (black circles) in lung fibrosis were more clearly delineated by hProCA32.collagen-enhanced MRI compared to nontargeted hProCA32 and Gadovist, while a direct

comparison of collagen enhancement with histological staining results is presented in Figure 5A. MRI enhancement with hProCA32.collagen-imaged fibrotic mice, especially in the subpleural region, was much greater for late-stage IPF than early-stage IPF. No honeycombing or traction bronchiectasis was observed in normal mice, while Gadovist could not detect honeycombing associated with late-stage IPF.

The specificity in the detection of the observed heterogeneous distribution of lung fibrosis was further revealed by detailed pixel analysis of the resulting MR images (Figure 3F−I). Injection of hProCA32.collagen resulted in changes in lung MRI SNR distribution for both early- and late-stage fibrosis, and the pixel distribution observed was heterogeneous for both early and late stage compared to the homogeneous distribution observed before and after injection of Gadovist in 6 weeks post-BM-treated mice (late-stage) and normal mice injected with hProCA32.collagen. These studies demonstrated the capability of hProCA32.collagen to specifically detect early- and late-stage lung fibrosis and its heterogeneity using multiple MRI pulse sequences.
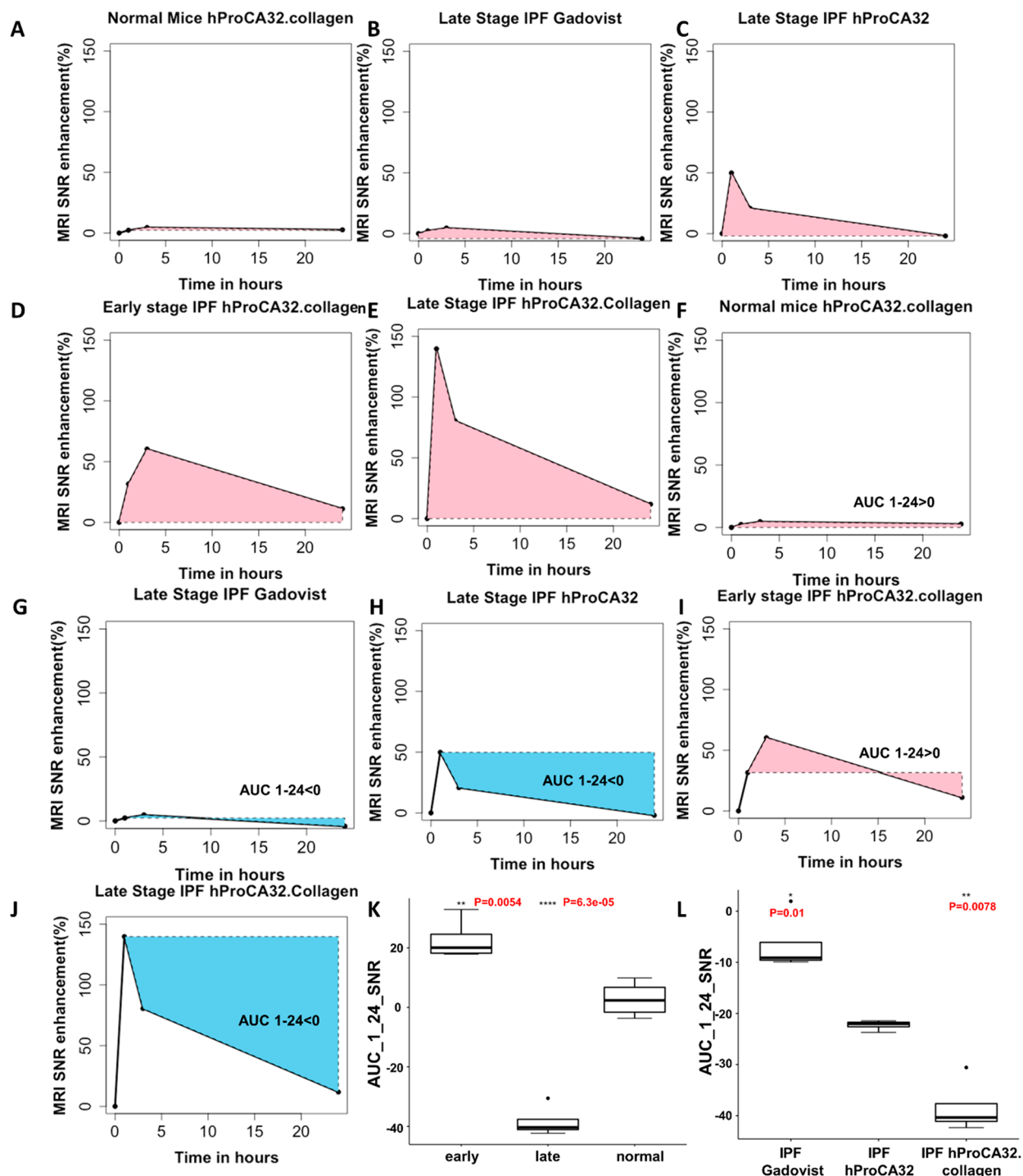
Figure 6. Lung enhancement pattern of healthy and BM-induced mice models. (A−C) AUC_0−24h SNR enhancement analysis provides an overview of various SNR enhancement performances for different groups of mice, including late-stage hProCA32.collagen normal mice, IPF Gadovist-injected mice, and IPF hProCA32 nontargeted mice. (D,E) AUC_0−24h SNR enhancement analysis demonstrates the capability of hProCA32.collagen to differentiate between late-stage and early-stage IPF by examining the SNR enhancement peak. The peak for the early stage occurs at 3 h, while the peak for the late stage occurs at 1 h. (F−H) AUC_1−24h SNR enhancement analysis demonstrates the capability to differentiate normal, late-stage IPF hProCA32, and late-stage IPF Gadovist by the AUC_1−24h value. The value of AUC is positive for both hProCA32-injected normal mice and Gadovist injection, but negative for hProCA32 injection. (I,J) AUC_1−24h SNR enhancement analysis shows the ability to further differentiate between IPF hProCA32 early stage and late stage by the AUC_1−24h value, with positive values for the early stage and negative values for the late stage. (K) AUC_1−24h boxplot analysis shows the ability of hProCA32.collagen to distinguish normal vs early stage vs late stage in the IPF model (*$P < 0.05$, **$P < 0.01$, unpaired two-tailed Student's t test). This result is considered statistically significant. (L) AUC_1−24h boxplot analysis demonstrating the ability of hProCA32.collagen to distinguish Gadovist vs nontargeted hProCA32 vs hProCA32.collagen in IPF model (*$P < 0.05$, **$P < 0.01$, unpaired two-tailed Student's t test; the boxplot shows the median of the data, with the upper and lower limits of the box representing the third and first quartile, and the whiskers extend up to 1.5 times the interquartile range to show the minimum and maximum as they are all within that distance).
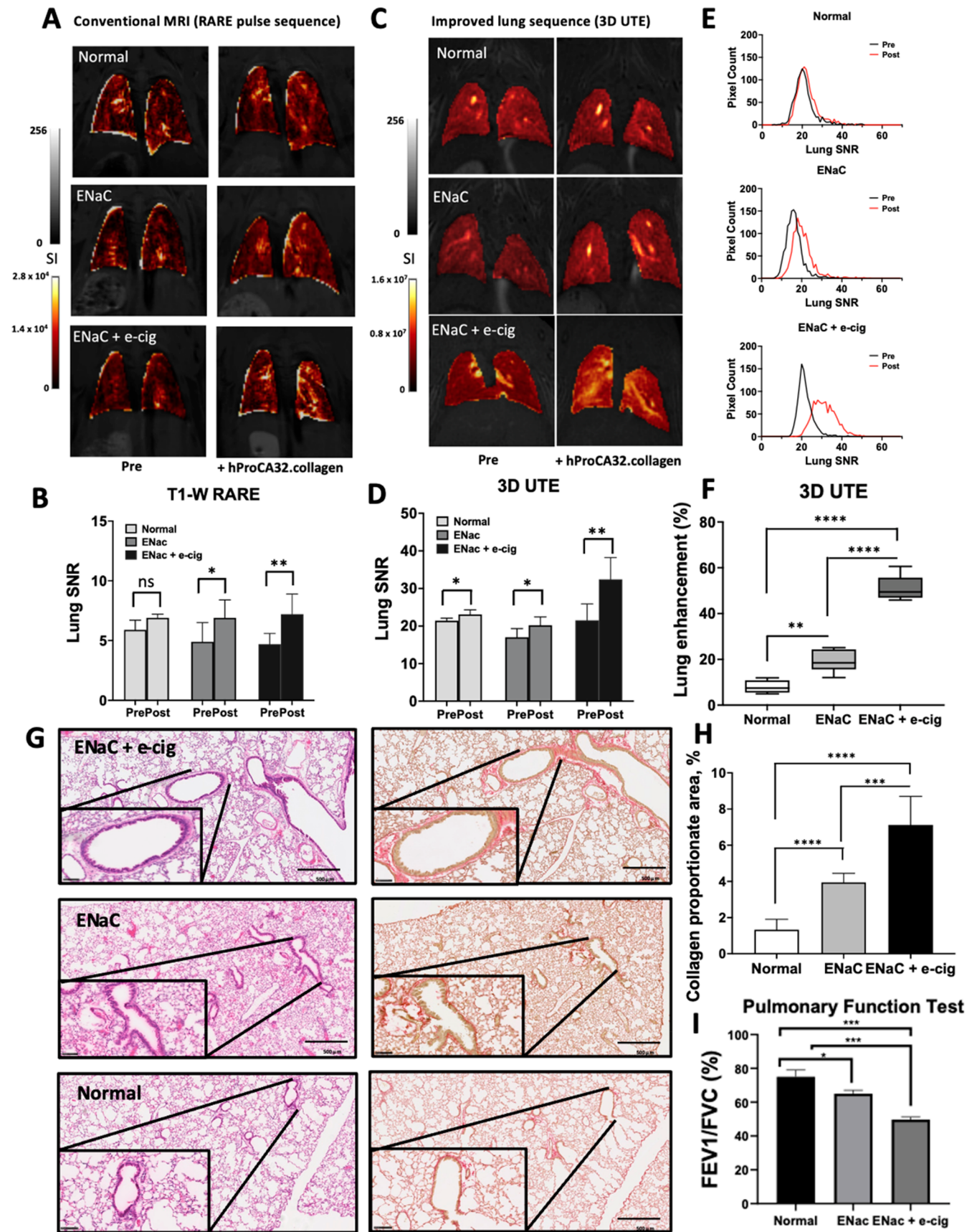
Figure 7. Detection of airway fibrosis in βENaC mice exposed to nicotine-containing E-cigarette vapor. (A) RARE (T_1-weighted) MRI of normal (healthy) mice, transgenic β epithelial sodium channel (βENaC) mice, and transgenic β epithelial sodium channel (βENac) mice with E-cigarette vapor (βENac + e-cig) before and 3 h after injection of hProCA32.collagen. (B) Lung SNR increase after injection of hProCA32.collagen. E-cigarette-exposed mice had a SNR increase significantly higher than that of healthy mice with an enhancement in the lung airways (blue arrow).

Figure 7. continued

(C) T_1-weighted 3D-UTE MRI of normal (healthy) mice, βENac mice, and βENac + e-cig before and 3 h after injection of hProCA32.collagen. (D) Lung SNR increases after injection of hProCA32.collagen. (E) Histogram pixel analysis of normal mice vs βENac mice vs E-cigarette mice model before and at peak enhancement (3 h) after injection of hProCA32.collagen by 3D-UTE pulse sequence. (F) Comparison of lung signal enhancement (%) in normal mice, transgenic ENaC mouse model, and nicotine-induced lung fibrosis ENaC model for COPD. (G) Histological analysis of E-cigarette-exposed mice compared to transgenic and normal non-E-cigarette-exposed vs normal mice showed increased collagen accumulation in the lung airways of E-cigarette-exposed mice by H&E staining and Sirius Red staining. A zoomed-in image of a black segment showed the collagen level around the airways on each histological slice. (H) Collagen proportional area (CPA) measured from SR-stained tissue. (I) Pulmonary function test of normal, βENac, and βENac with E-cigarette-vapor-exposed mice indicated a significant decline in lung function compared to control. All data are shown as mean $\pm$ SD, $n = 4$ biologically independent animals in each group, *$P < 0.05$, **$P < 0.01$, ***$P < 0.001$, ****$P < 0.0001$ Student's t test; MR image scales represent signal intensities.
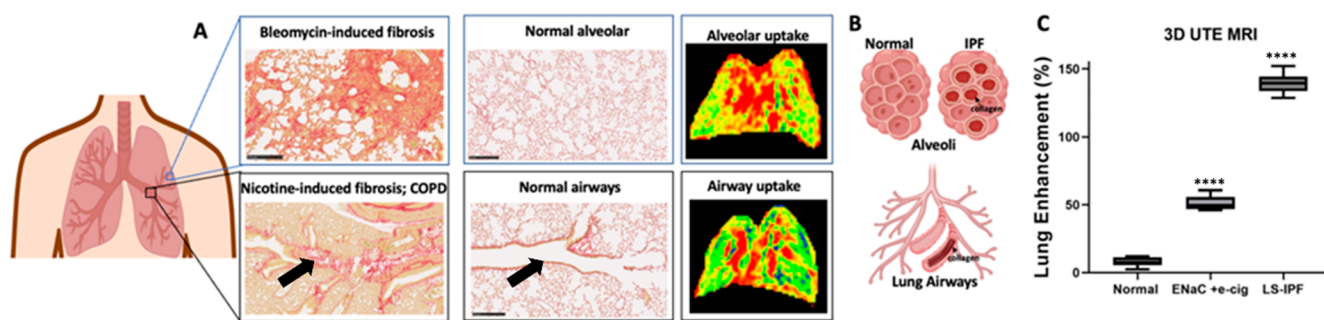
Figure 8. Comparison of collagen accumulation pattern and hProCA32.collagen pattern uptake in BM-induced IPF and E-cigarette-induced lung fibrosis in COPD mouse models. (A,B) Collagen accumulation and binding in IPF and COPD with overexpression of collagen 1 (red color) at alveolar and the bronchial airways, respectively, compared to normal healthy mice (middle panel). Human collagen-targeted protein MRI contrast agent (hProCA32.collagen)-detected collagen overexpression in IPF and COPD at the alveolar (top) and bronchial airways (bottom) in 3D-UTE MRI. (C) Comparison of lung signal enhancement (%) in normal mice, nicotine-induced lung fibrosis model for COPD, and bleomycin-induced mice model (LS, late stage; ****$P < 0.001$ one-way ANOVA).

2.3. Molecular Dynamic Imaging Enhancement with Strong Detection Sensitivity and Specificity

To better understand the heterogeneity features observed, we compared MRI lung enhancement enabled by hProCA32.collagen, nontargeted hProCA32, and Gadovist as a function of time. hProCA32.collagen injection to early-stage mice with 3 weeks BM treatment resulted in MR image enhancement from 10.5 ± 0.4 at pre-injection to 13.8 ± 0.3 after 1 h and 16.8 ± 0.4 after 3 h post-injection, representing increases of 31.6 and 60.0%, respectively. Interestingly, hProCA32.collagen injection in the late-stage set of mice treated with bleomycin for 6 weeks resulted in a 139.0% enhancement and signal retention up to 80.5% at 1 and 3 h time points. The enhancement then decreased and washed out over a longer period of time. The MRI enhancement was reduced to 10% at 24 h post-injection (Figure 6E). No significant MRI enhancement was detected in tissues with lung fibrosis 48 h post-injection. In contrast, no significant changes were observed in the lung SNR of either normal mice with hProCA32.collagen or Gadovist-injected late-stage IPF mice. A characteristic percentage change in SNR values of ~50% was observed for late-stage IPF mice injected with nontargeted hProCA32 (Figure 6C). These results indicated that while nontargeted hProCA32 was also able to detect lung abnormality associated with late-stage IPF at 1 h, collagen-targeted hProCA32.collagen provided ~3-fold higher enhancement at 1 h due to a combination of blood pool and targeted (collagen) binding. As seen in Figure 5A,B, the "retained" enhancement at 3 h post-hProCA32.collagen injection, presumably due to the slow off-rate of specific binding of fibrosis via hProCA32.collagen, exhibited a pattern similar to those observed in Sirius Red and Masson Trichrome staining. Furthermore, fibrotic lesions corresponded linearly to

Sirius Red lesions with an R^2 of 0.86. The AUC_0−24 analysis for healthy, early-stage, and late-stage IPF mice (Figure 5C−F) demonstrated a significant linear correlation with *ex vivo* hydroxyproline content and histology analysis for the collagen area (Figure 5C), hydroxyproline content (Figure 5D), collagen area (Figure 5E), and Ashcroft score (Figure 5F). Thus, using the dynamic enhancement post-injection of hProCA32.collagen as a function of time provided excellent distinction in detecting early and late stages of lung fibrosis (Figure 6).

2.4. Detection of E-Cigarette-Induced Lung Fibrosis in a COPD Mouse Model by hProCA32.collagen

To further demonstrate the precision MR imaging capability of detecting lung fibrosis by hProCA32.collagen, we employed a second animal model of nicotine-containing electronic (e)-cigarette-induced COPD[22] (Figure 7). We used βENaC-overexpressing mice bearing COPD-like pulmonary abnormality and exposed them to an electronic nicotine delivery systems (ENDS). The Sirius Red staining and hydroxyproline assays showed that ENDS-exposed mice displayed enhanced fibrotic phenotypes, with collagen overexpression in the small airways and vascular structures of the lungs, compared to control mice (Figure 7G,H). Like COPD patients, the mice displayed a marked decrease in FEV1/FVC ratio compared to healthy and nonexposed mice (Figure 7I).

2D RARE MR images of an E-cigarette mice model indicated an appreciable increase in the lung density and hence SNR values compared to both normal and transgenic mice with no E-cigarette exposure, while 3D-UTE MR images revealed an increase in lung MRI signal at the lung bronchi (Figures 7A−D). The enhanced MRI signals then decreased over a longer time due to the excretion of the contrast agent

(data not shown). The observed heterogeneous pixel distribution (Figure 7E) confirmed the detection capability by pMRI with hProCA32.collagen. This was further confirmed by H&E staining as well as Sirius Red staining, with collagen deposition in the airway (Figure 7G,H).

Figure 8 shows the MRI detection of lung fibrosis with collagen expression for both BM-induced IPF and E-cigarette-induced COPD fibrotic model. pMRI with hProCA32.collagen enabled the observation of differential lung MRI enhancement patterns for both animal models in the alveolar and bronchi for BM-induced and E-cigarette-induced models, respectively. Marked differences were also observed in collagen expression BM-induced lung fibrosis at the alveolar region versus E-cigarette induced COPD fibrotic model in the lung bronchi (black arrow). COPD mice with lower collagen expression (5−6%) had lower hProCA32.collagen-enabled lung MRI enhancement compared to IPF.

2.5. Tissue Distribution and Toxicity

The biodistribution of Gd^{3+} after intravenous (i.v.) injection of hProCA32.collagen (0.025 mmol/kg of body weight) was measured with ICP-OES using *ex vivo* mouse tissue harvested at 1 and 14 days after injection. The samples were analyzed with ICP-OES to quantify hProCA32.collagen concentration at the analyzed time points. The biodistribution and concentration of hProCA32.collagen (by Gd^{3+} concentration measurement) by ICP-OES seen in Figure S7 is consistent with MRI analysis. Minimal residual Gd^{3+} was observed in the organs, including bone and brain, which has been a major cause of concern associated with some clinical contrast agents (Figure S7A).

Acute toxicity, measured with liver enzymes (ALT, ALP), urea nitrogen, bilirubin, and total protein from CD-1 mice, 48 h after tail vein injection of hProCA32.collagen (0.025 mmol/kg) and PBS, was analyzed. In addition, blood samples were collected from the mice 14 days post-injection. The blood from CD 1 mice injected with PBS was used as the control. Based on the results from IDEXX laboratories from 3 mice in each group, all the tests, including creatine, ALT, ALP, cholesterol, and triglycerol, had similar values between the control group and the group injected with hProCA32.collagen. In addition, the values were within the normal range reported for these tests. This indicated that the function of the organs, including the kidney and liver, were not altered by the injection of hProCA32.collagen (Figure S7B).

Tissues from different organs of the mice were collected for detailed examination. No significant differences were observed between the appearance and weight of the tissue specimen for the PBS-injected cohort compared to hProCA32.collagen-injected mice (Figure S8A,B). No tissue toxicity associated with hProCA32.collagen was observed in any of the selected tissues (Figure S8C). Collectively, these toxicity tests confirmed that hProCA32.collagen did not result in tissue or cytotoxicity.

3. DISCUSSION

Idiopathic pulmonary fibrosis is the most common type of idiopathic interstitial pneumonia and occurs with as much frequency as brain, stomach, and testicular cancer.[23] While high-resolution computed tomography scanning has proven invaluable in diagnosing the disease and currently represents a gold standard for detection, this method has poor soft tissue contrast and cannot detect early-stage lung fibrosis. It is only used as entry criteria into clinical trials due to large interobserver variation, and interpretation of HRCT data can vary significantly (up to 50%) during diagnosis.[6,7] Additionally, surgical lung biopsies in patients with suspected IPF often have high sampling error, physical impairments, and comorbidities that make biopsy risky.[9,10]

Progress in selecting patients for lung transplantation and other treatments has been constrained by a lack of noninvasive and longitudinal diagnostic methods, and methods for monitoring disease progression. Pirfenidone and nintedanib have been approved for treating IPF in the U.S.[24,25] but have demonstrated limited efficacy in preventing disease progression and improving quality of life, and may present tolerability issues.[26] The importance of early diagnostics of IPF and direct detection of heterogeneous expression of fibrosis was highlighted when these two drugs were shown to have some effect on functional decline and disease progression and reduced long-term mortality for patients with mild to moderate IPF. Further tracking of disease progression and monitoring clinical trials is problematic, and physiological changes are only noted with acute exacerbations. Currently, there are no effective therapies capable of targeting these underlying fibrotic changes in the lung, despite efforts directed toward developing antifibrotic therapies and many clinical trials.[27] There is a pressing need to develop noninvasive imaging methodologies to enable early detection of fibrosis, longitudinally quantify lung fibrosis for staging during progression and regression upon treatment, facilitate patient selection for precision medicine, and improve preclinical drug discovery.[2,28]

IPF is characterized by increased extracellular matrix deposition with overexpression of collagen, the main type I collagen in the lung, which causes a decline in lung function with either impaired gas exchange and parenchymal consolidation or nonreversible airway obstruction. Thickening of the lamina reticularis leads to decreased airway elasticity and, thus, increased airway limitation. Quantification of collagen expression levels has been commonly used as a gold standard for staging lung fibrosis, including IPF for both patients and animal studies.[17,29,30] Results of this study demonstrate in both patient tissue samples and animal models that collagen I is highly expressed in IPF (up to 10−20 μM concentrations), and its expression level is stage-dependent (Figures 1C and 2). From Figures 1C and 2B, it can be seen that while collagen deposition within the lung tissue occurs in IPF, the location of the deposits and etiology often differ. Thus, collagen I is an ideal biomarker for early and accurate detection of lung fibrosis and monitoring its progression and regression quantitatively.[17,30] Unfortunately, this early-stage pathological collagen expression occurs much sooner than lung architectural distortion can be detected by HRCT since CT only detects architectural changes in lung tissue. CT-opaque pulmonary edema during the inflammatory phase also limits the detection of early-stage IPF by CT. In addition, HRCT and other diagnostic methods available provide little information about heterogeneous fibrosis related to disease activity and progression.[8,31]

MRI has been explored as an imaging modality for early detection and monitoring of lung disease progression[32,33] due to its advantage of not using harmful ionizing radiation, superior ability to characterize tissue properties, and dynamic image acquisition capacities. However, lung imaging by MRI, especially in small animals, presents some unique challenges.[34,35] First, the relatively low tissue density (10×

lower) and associated low water content within the lungs severely limit signal-to-noise. In addition, variations in magnetic "susceptibility", associated with the many air–tissue interfaces of the alveoli and bronchioles, create local magnetic field inhomogeneities (field gradients) that can lead to shortening some relaxation times. Further, respiratory and cardiac motion can lead to significant image blurring. Studies have reported that He gas and ^{129}Xe-based hyper-polarized MRI can distinguish between normal and diseased lung tissue,[36] but this method lacks a renewable thermal signal. The collagen-targeted contrast agent Gd-DTPA (Magnevist) (EP-3533) has been used to observe images of lung fibrosis at a late stage with improved sensitivity and specificity.[17] To overcome limitations of linear chelators such as DTPA used in EP3533, including low in vivo metal stability and association with Gd^{3+} retention in the bone, and constraints of translational applications,[37] an oxyamine-functionalized derivative of Gd-DOTA has been developed to target allysine in oxidized collagen.[38,39] Caravan also reported an aldehyde-binding MRI probe Gd-Chyd to target lung fibrogenesis[40] and an allysine-binding PET probe ^{68}Ga-NODAGA indole.[41] A DOTA-based collagen targeted PET contrast agent was recently evaluated with rodents and IPF patients;[28,42,43] however, a histological validation to understand its target specificity has yet to be demonstrated. While Gadofosveset (Ablavar), an FDA-approved, gadolinium-based, albumin-binding contrast agent, has detected albumin extravasation in subjects with pulmonary fibrosis with tissue injury by MRI, it is not clear whether some component of these findings could be explained by very early fibrotic changes or neovascularization.[44]

Our laboratory has pioneered a new class of protein-based Gd^{3+}-based contrast agents by creating Gd^{3+} binding sites in a scaffold protein, such as rat Parvalbumin (ProCA32), to systematically optimize relaxivity, metal binding, specificity, targeting capability, and imaging properties.[12] By engineering a biomarker targeting moiety to ProCA32 with a flexible hinge, biomarker-targeted contrast agents exhibit similar relaxivity and metal binding capability to ProCA32. It also has the added capability to selectively bind and quantify the desired biomarkers overexpressed in chronic diseases, such as collagen (rProCA32.collagen), for noninvasive early detection of liver fibrosis and liver metastasis in several mouse models.[11,16] Here, we report the development of human collagen-targeted protein MRI contrast agent (hProCA32.collagen) to specifically bind to collagen I overexpressed in multiple lung diseases, to address the clinical reliance in human subjects and the pressing unmet medical needs associated with pulmonary fibrosis. We hypothesized that hProCA32.collagen could enable early and accurate detection of lung fibrosis with disease activity using pMRI. The findings reported here have several important implications. The developed human collagen-targeted contrast agent has advantages over our previously reported rat collagen-targeted agent with less immunogenicity concern.[11,16] Here, we also demonstrated that hProCA32.collagen has strong specificity to human collagen type I with strong translational capability of hProCA32.collagen for detection of human lung fibrosis. We reported the first detection of early- and late-stage lung fibrosis with stage-dependent MRI signal-to-noise ratio increase using a newly established progressive bleomycin-induced IPF mouse model, as well as the detection of fibrosis in the lung airway of an electronic cigarette-induced COPD mouse model.

The contrast agent hProCA32.collagen has significantly improved r_1 and r_2 relaxivity at both low and high magnetic field strengths compared to r_1 (6.5 mM^{-1}·s^{-1}) and r_2 (8.7 mM^{-1}·s^{-1}) of current clinical contrast agents. hProCA32.Collagen exhibits high relaxivity values for both r_1 (32.0 ± 0.3 mM^{-1}·s^{-1}) and r_2 (51.0 ± 0.2 mM^{-1}·s^{-1}) per Gd^{3+} at 1.4 T, and r_1 (18.5 ± 1.5 mM^{-1}·s^{-1}) and r_2 (105.6 ± 2.0 mM^{-1}·s^{-1}) at 7.0 T, at 37 °C (Figure 1E).[18,19] hProCA32.collagen also has a strong Gd^{3+} binding affinity comparable to rProCA32.collagen and DTPA (Table 1).[13] Importantly, it exhibits strong metal specificity with ∼10^{11}-fold metal selectivity for Gd^{3+} over physiological metal ions such as Zn^{2+} (Table 1). Additionally, hProCA32.collagen remains stable in serum with strong transmetalation resistance compared to clinically approved stable Gd^{3+} contrast agents such as Dotarem and ProHance (Figure 1). Furthermore, minimal residual Gd^{3+} was detected in mouse organs, and no acute toxicity was observed (Figures 1 and S7 and S8). With the injection dose of hProCA32.collagen for in vivo imaging 40-fold lower than clinical contrast agent Gadovist, hProCA32.collagen is expected to have a strong potential to mitigate metal toxicity for translation applications.

Contrast agent hProCA32.collagen has a strong binding affinity to type I collagen, with a K_d of 0.18 ± 0.02 μM (Figure 1b) determined by ELISA, which makes it sensitive to the pathological concentrations of overexpressed collagen I (∼10–20 μM concentration).[15−17] hProCA32.collagen also binds other types of collagens, such as types III and IV, which are expressed in chronic lung diseases but with much lower binding affinities[16] (Figure S2). Importantly, immunostaining analysis revealed that hProCA32.collagen binds to human collagen in patient lung fibrosis tissue samples with a collagen pathological pattern similar to that of Sirius Red staining, with an excellent correlation (Figure 1C), demonstrating the strong translational capability of hProCA32.collagen for detection of human lung fibrosis.

Bleomycin treatment frequently causes decreased lung volume and induces honeycombing conditions seen in HRCT scans, typical of interstitial lung diseases such as IPF.[17,45] A commonly used transtracheal injection, bleomycin-induced lung fibrosis, has limitations due to a lack of human disease features.[30] To ensure close mimicry of human lung fibrosis in IPF, we have developed an IPF model using I.P. injection of bleomycin, as this method is more physiologically relevant with UIP pattern and honeycombing in IPF patients in comparison to transtracheal administration previously used in animal models (Figure 2). We have characterized and staged this mouse model of lung fibrosis progression using the Ashcroft scores and established a scoring function of collagen area. As verified by Sirius Red stain, Masson Trichrome stain, and measuring various fibrosis markers including collagen levels,[46,47] lung fibrosis development and progression at an early stage and late stage can be induced at 3 and 6 weeks by I.P. injection of bleomycin sulfate. It has also been reported that antifibrotic drugs can effectively reduce collagen expression in this animal model.[30]

Here, we report the first robust detection of early and late-stage lung fibrosis by hProCA32.collagen using this newly established progressive bleomycin-induced IPF mice model. hProCA32.collagen enables the detection of early and late-stage IPF, with stage-dependent MRI SNR increase, exhibiting good sensitivity and specificity using several imaging methodologies, including UTE and RARE imaging pulse sequences (Figures 3 and 4). 3D-UTE was utilized to overcome the

challenge of the very short echo time (TE) of the lungs and artifacts in lung fibrosis generated from animal respiration, and Radial sampling reduces TE. Results demonstrated that hProCA32.collagen accumulated within the alveoli of the ECM-remodeled mouse lung generated MRI signals that correlated linearly with the collagen area obtained by histological analysis and hydroxyproline content of the lungs. In comparison with the imaging enhancement of nontargeting hProCA32 in normal mice, histological analysis and radiographic correction revealed that the lung MRI signal enhancement observed with hProCA32.collagen for the early and late stage of IPF was largely attributed to collagen binding (Figures 3−5). In contrast, the clinically approved MRI contrast agent Gadovist did not improve lung MRI enhancement. hProCA32.collagen can also selectively bind fibrotic lung tissues with pulmonary hypertension in late-stage models containing a high accumulation of type I collagen, resulting in delayed clearance observed as retained MR signal enhancement at the 3 h time point (Figures 3J and 6E). This finding points to the applicability of hProCA32.collagen in distinguishing healthy lungs from fibrotic lungs at different late stages.

We further report the first detection of lung fibrosis by hProCA32.collagen and pMRI using an E-cigarette-induced COPD mouse model (Figures 7 and 8). βENaC-over-expressing mice exhibited COPD-like pulmonary abnormality following exposure to ENDS. Enhanced fibrotic phenotypes with collagen overexpression in the small airways and vascular structures of the lungs were revealed by Sirius Red staining and hydroxyproline assay. Consequently, the mice displayed a marked decrease in FEV1/FVC ratio, like COPD patients, compared to healthy and nonexposed mice (Figure 7I). Importantly, ~50% lung MRI enhancement by ProCA32.collagen was detected using both 3D-UTE and conventional RARE imaging methodologies. This enhancement is largely due to collagen binding, verified by histological analysis and comparison with non-E-cigarette-exposed mice and normal mice. Lung enhancement of MRI signal from mice exposed to E-cigarette smoke by hProCA32.collagen is significantly greater than nonexposed transgenic mice and normal mice, respectively, which correlates well to their corresponding collagen overexpression levels (CPA%), as well as lung function test results (Figures 7 and 8). The detected MRI lung signal enhancement was found to correspond to the *ex vivo* histological images (Figure 7G), showing morphological airway abnormalities and increased collagen accumulation, confirmed by collagen area quantification. Thus, these results demonstrate the strong potential for noninvasive imaging of lung fibrosis with collagen expression in the lung bronchi (black shape Figure 7) by hProCA32.collagen with pMRI. Considering the lung imaging of fibrosis in both IPF and COPD mouse models (Figure 8), these results confirm that the designed collagen-targeted MRI contrast agent has specific uptake and specificity to collagen regardless of the location of collagen accumulation.

We also previously reported that the rat analogue ProCA32.collagen1 enables robust detection of early-stage (Ishak stage 3 of 6) liver fibrosis, nonalcoholic steatohepatitis (Ishak stage 1 of 6 or 1 A Mild), and liver metastasis, in animal models via dual contrast modes.[11] The current results of hProCA32.collagen for a sensitive, specific, and precise noninvasive method to target excess collagen deposition in the lungs of IPF and COPD patients, regardless of the stage, represent another major leap in molecular imaging. An

important element of these findings is that compared to current clinical and research-based contrast agents, molecular imaging using hProCA32.collagen may be an essential tool for monitoring treatment response and possibly providing a prognostic value in human lung fibrosis and other collagen-related diseases, including the tumor microenvironment of lung cancer. It also has strong potential applications in facilitating drug discoveries for IPF and COPD by longitudinal and precise imaging of the same objects in quantifying collagen expression in fibrosis progression and treatment.

One of the potential limitations of our collagen-targeted MRI contrast agent is its relatively longer retention time compared with clinically approved contrast agents based on small chelators. This raises a concern regarding the potential for Gd^{3+} toxicity despite its 40-fold reduced injection dose compared with Gadovist, and strong metal selectivity and specificity for Gd^{3+} over endogenous metal ions such as Ca^{2+} and Mg^{2+}. Further PK analysis of retention time and biodistribution as well as formulation studies to reduce the retention time may be beneficial to address this concern.

There are certain challenges related to lung MR imaging. First, motion artifacts from breathing can inhibit visualization of the lungs and lead to difficulty in diagnosis of lung diseases. In addition, the relatively lower proton density in the lungs compared with other tissue results in loss of MRI signal. The air−tissue interface in the lungs also causes large magnetic susceptibility gradients that cause signal loss in these types of pulse sequences. Here, we have shown that a UTE MRI method can overcome this limitation and produce positive signals in the lungs. The UTE method is a self-gated spoiled gradient echo acquisition strategy that uses a 3D radial pseudo randomized sampling scheme with variable density read-out trajectories. This allows for retrospective respiratory self-gating technique and removal of intermittent bulk motion in free breathing. This method can be used for the imaging of pulmonary and cardiac tissue pathologies at high isotropic resolution without affecting signal loss in the lung parenchyma due to shorter T_2^*. The repeated sampling scheme of the k-space center mitigates the motion artifacts and enables tracking of bulk and respiratory motion.[48] It is possible that the required detection dose can be further reduced once we have optimized imaging methodology to reduce motion artifacts by further incorporating the retrospective self-gating along with UTE method.

Various efforts using single photon emission computed tomography (SPECT) or positron emission tomography (PET) for the detection of rodents and IPF patients[42] have also been reported to address this currently unmet imaging need,[41,38,41,49,50] including an allysine-binding PET probe ^{68}Ga-NODAGA indole,[41] and a DOTA-based collagen-targeted PET contrast agent that was recently evaluated with rodents and IPF patients.[28,42] Our developed collagen-targeted MRI contrast agent exhibits several major advantages over PET agents and CT, including: (i) higher tempo-spatial resolution during disease progression and regression in treatment from frequent longitudinal imaging and quantification of collagen expression levels without radiation exposure; (ii) reduced safety concerns with more accessibility to patient populations, including children and pregnant women; and (iii) broader application due to greater accessibility of MRI and lower demand for instrumentation, maintenance, and personal costs.

4. METHODS

4.1. Protein Expression, Purification, and PEGylation of hProCA32.collagen

To address the clinical relevance of the design of hProCA32.collagen contrast agent in human subjects, a human protein scaffold was used in place of the previously reported rat analog ProCA32.collagen1.[11] A streak of the glycerol stock was incubated in a 5 mL LB medium using an inoculation tube, and then allowed to grow overnight at 37 °C, 220 rpm. The inoculum was stored at 4 °C for about 8 h to stunt growth and maintain stability until it was transferred into 100 mL ampicillin LB. This was then grown overnight at 37 °C, 220 rpm. The resulting inoculum was transferred into 250 mL LB media and grown overnight as previously described, and the medium was used as the small-scale medium for transfer into large scale. 35 mL was transferred per liter, and optical density (OD) was monitored at 600 nm until OD_{600} reached ∼0.6, after which 0.25 mM IPTG was added for induction of protein expression, and the temperature was then reduced to 25 °C for overnight growth. The cell pellet was obtained by centrifugation at 7000 rpm for 40 min at 4 °C. The purification of hProCA32.collagen followed an established protocol with slight modification.[12] SDS-PAGE confirmed that the purified hProCA32.collagen was PEGylated using methoxy PEG succinimidyl carboxymethyl ester for amine PEGylation with a molecular weight of 2 kDa (JenKem Technology). Unreacted PEG was removed by an Amicon stirred concentrator (EMD Millipore) using a 3 kDa filtration membrane. PEGylated products were confirmed by SDS/PAGE with protein staining Coomassie Brilliant blue.

4.2. Patient Samples Stained by Collagen-Targeted Contrast Agent and Sirius Red

Lung adenocarcinoma with matched normal adjacent tissue and lung tissue (formalin-fixed paraffin-embedded), each containing 24 cases of lung tumor tissues from autopsy, duplicated cores per case, were purchased from US Biolab, Inc., catalog #LC10013B, and used to stain for collagen and ProCA32.collagen1. Each slide had 48 cores, 24 cases, with core diameters of 1.5 mm and thickness of 5 μm. In this procedure, the contrast agent was incubated with the ProCA32.collagen1 antibody (antigen purified polyclonal rabbit anti-ProCA32 antibody) in a 1:2 ratio, then the mixture was added at a final concentration of 50 μg/mL of contrast agent, and the preincubated mixture was added into the slides overnight at 4 °C. DAB chromogen was used to develop the stain, and each slide was counter-stained with hematoxylin. Representative images of 6 cores stained for contrast agent and Sirius Red on adjacent slides are seen in Figure 1C. The CPA, as determined by the % area stained with Sirius Red, was quantified from the histology images using ImageJ as per standard procedures.[11] The percentage of Sirius Red-stained areas was calculated based on the entire slide scan. The results are mean values across 10 different cores from different lung arrays. Linear regression with $R^2 = 0.9678$ ($P < 0.0001$) showed the linear relationship between hProCA32.collagen-stained human tissue versus Sirius Red.

4.3. Development of Animal Models

4.3.1. Bleomycin-Induced Pulmonary Fibrosis.
All animal experiments described were performed in accordance with National Institutes of Health (NIH) guidelines for the care and use of laboratory animals and were approved by the institutional animal care and use committees (IACUCs) of Georgia State University, Emory University, and the University of Georgia.

Eight-week-old male C57BL/6 mice were given an intraperitoneal injection of 25 mg/kg bleomycin sulfate twice weekly. To induce different stages of lung fibrosis, bleomycin induction lasted for 3, 4.5, and 6 weeks, to induce early, moderate, and late stages, respectively. One week after stopping bleomycin treatment, the mice were taken for MRI analysis. The lungs were harvested and weighed and then saved for the following hydroxyproline assay and histology examinations. For histology, lung sections were prepared after formalin inflation and fixation, embedded in paraffin, and stained with hematoxylin and eosin (H&E), Sirius Red staining, and immunohistochemistry for α-SMA and arginase-1.

4.3.2. E-Cigarette-Induced COPD.
To induce a phenotypic response akin to human COPD, C57BL/6J-βENaC-Tg, containing an overexpression of the sodium channel nonvoltage-gated 1 beta subunit (Scnn1b), mice were exposed to nicotine-containing (12 mg/mL) E-cigarette vapor for 30 min a day, 5× per week for 8 weeks. Mice underwent MR imaging 24 h after their last E-cigarette vapor exposure. Following MR imaging, pulmonary function analysis was completed by flexiVent and animals were euthanized.

4.3.3. Histological and Immunohistochemical Analysis.
The lung was inflated with 4% neutral buffered paraformaldehyde, and then fixed in fresh 4% neutral buffered paraformaldehyde for 24 h and embedded in paraffin. The tissue blocks were sliced into 6 μm sections and stained with H&E and Sirius Red stain.

For immunohistochemistry, the tissue sections were deparaffinized and rehydrated using a graded ethanol series. Antigen retrieval was performed with citrate buffer (pH 6.0). Then the endogenous peroxidase activity was blocked by 0.2% hydrogen peroxide for 10 min. After blocking in 2% goat serum for 20 min, sections were incubated with rabbit anti-α-SMA antibody (Abcam) overnight at 4 °C. The sections were then incubated with HRP-linked polymer and counterstained with hematoxylin. The slides were analyzed under a Keyance microscope. The Sirius Red staining was performed using NovaUltra Sirius Red Kit (IHC World). After the tissue sections were deparaffinized and rehydrated, the sections were incubated with hematoxylin for 8 min, followed by 10 min washing in tap water. The sections were incubated with picro-Sirius Red for 1 h, followed by washing in acidified water. The slides were analyzed under a microscope.

4.3.4. MRI Scan.
The first cohort of bleomycin-treated mice ($n = 2$ per group) were selected for confirmation of IPF development and were imaged on a 7 T Agilent MRI scanner at the Biomedical imaging research center (BIRC) of the University of Georgia. Animals were anesthetized by isoflurane inhalation, and their respiration rate and temperature were monitored with a rodent physiological monitoring system while maintaining the breathing rate of the mouse at 65 to 70 breathes per minute (BPM). MRI scans were obtained before and after injection of 0.0025 mmol/kg nontargeted hProCA32 or hProCA32.collagen and 0.1 mmol/kg Gadovist. Two-dimensional spin echo multislice (T_1-weighted images) were collected with the following acquisition parameters: TR = 500 ms, TE = 15 ms, Segment/ETL = 32/8, FOV = 40 × 40 mm, matrix = 256 × 256, total image slices = 8, slice thickness = 1.0 mm without gap. Fast spin echo multi slices (T_2-weighted images) were obtained with the same parameters as above except the following parameters: TR = 2000 ms, effective TE = 40 ms.

The second cohort of bleomycin-treated mice and E-cigarette-induced fibrotic mice (n = 3 per group) were imaged on a 7.0 T Bruker scanner at Yerkes National Primate Research center at Emory University. The anesthesia and mouse monitoring procedures are the same as outlined above. Lung Fibrosis was imaged with T_1-weighted 3D ultrashort TE MRI. 3D-UTE was utilized to overcome the challenge of the very short TE of the lungs and artifacts in lung fibrosis generated from animal respiration. Furthermore, radial sampling was applied to reduce TE.[51,52] With TR = 12 ms, TE of 0.16 ms, FOV was 48 mm × 48 mm, and matrix size was 192 × 192. T_1-weighted rapid acquisition with refocused echo MR sequence was used with the following parameters: TR = 300 ms, TE = 10.7 ms, FOV = 35 mm × 35 mm, matrix = 192 × 192, total image slices = 8, slice thickness = 1.0 mm without a gap.

The third cohort of transgenic ENaC mice and E-cigarette-induced fibrotic ENaC mice ($n = 2$ per group) were imaged on a 7.0 T Bruker scanner at Advanced Translational Imaging Facility (ATIF) at Georgia State University. The anesthesia and mouse monitoring procedures are the same as outlined above. Lung fibrosis was imaged with 3D ultrashort TE (3D-UTE) MRI. The parameters of 3D-UTE pulse sequence were as follows: TR = 5.176 ms, TE = 0.007 ms, FOV was 32 mm × 32 mm × 32 mm, and matrix size was 128 × 128 × 128. T_1-weighted rapid acquisition with refocused echo MR sequence was

used with the following parameters: TR = 500 ms, TE = 7.41 ms, FOV = 32 mm × 32 mm, matrix = 128 × 128, total image slices = 14, slice thickness = 1.0 mm without a gap.

4.3.5. Metal-Binding Affinity Studies. hProCA32.collagen is intended for use as a chelating agent for Gd^{3+} in MR imaging. It is therefore pertinent to estimate the binding affinity of physiological ions with charge and ionic radii similar to Gd^{3+}, as well as to ascertain the complex strength of hProCA32.collagen bound to Gd^{3+}. To do this, a metal-buffer system was developed. Due to the lack of spectroscopic signal for Gd^{3+}, the binding affinity to hProCA32.collagen was determined based on Tb^{3+} LRET experiments in which 30 μM hProCA32.collagen was prepared in 50 mM HEPES, 5 mM DTPA, and 150 mM NaCl at pH 7.2. The protein-Tb^{3+} LRET emission spectra were obtained for wavelengths between 520 to 580 nm, and at excitation wavelength of 280 nm. The free Tb^{3+} concentrations (Tb_{free}) at each titration point were calculated using eq 1. The dissociation constant of Tb^{3+} bound hProCA32.collagen ($K_{d\ Tb,ProCA}$) was subsequently calculated by the Hill equation (eq 2).

$$[Tb]_{Free} = \frac{K_{d\ Tb,DTPA}[Tb - DTPA]}{[DTPA]_{Free}} \quad (1)$$

$$f = \frac{[Tb]_{Free}^{n}}{K_{d\ Tb,ProCA}^{n} + Tb_{Free}^{n}} \quad (2)$$

where $[Tb^{3+}]_{free}$ is the free Tb^{3+} concentration obtained from the buffer system, $K_{d\ Tb,DTPA}$ is the dissociation constant of Tb^{3+} from DTPA, $[Tb-DTPA]$ is the concentration of Tb-DTPA complex formed during titrations, $[DTPA]_{free}$ is the free DTPA in the buffer, f is the fractional change of the LRET signal at each titration point, n is the Hill number, and $K_{d\ Tb,ProCA}$ is the dissociation constant of Tb^{3+} from hProCA32.collagen. The dissociation constants used for Tb^{3+} to DTPA were obtained from the National Institute of Standards and Technology Standard Reference Database.[53]

By competing Tb^{3+} with Gd^{3+}, Tb^{3+} fluorescence spectra were recorded by tryptophan excitation at 280 nm, and emission was recorded from 500 to 650 nm. 10 μM hProCA32.collagen and 20 μM Tb^{3+} were incubated with different concentrations of $GdCl_3$ from 0 to 1000 μM at room temperature overnight. The Tb^{3+}-FRET changes were recorded at an emission of 545 nm. The apparent dissociation constants ($K_{d\ app}$) were calculated by fitting the plot of LRET peak intensities over different concentrations of Gd^{3+} in eq 3 and the dissociation constants of Gd^{3+} to hProCA32.collagen ($K_{d\ Gd,ProCA}$) were subsequently calculated using eq 4, where:

$$f = \left\{ ([Tb]_T + [Gd]_T + K_{d\ app}) - \sqrt{([Tb]_T [Gd]_T + K_{d\ app})^2} \right.$$
$$\left. - 4X[Tb]_T X[Gd]_T \right\} / 2X[Tb]_T \quad (3)$$

$$K_{d\ Gd,ProCA} = K_{d\ app} X \frac{K_{d\ Tb,ProCA}}{K_{d\ Tb,ProCA} + [Tb]_T} \quad (4)$$

f is the fractional change of the LRET signal,[54] $[Tb]_T$ is the total Tb^{3+} concentration, $[Gd]_T$ is the total Gd^{3+} concentration at each titration point, and $K_{d\ Gd,ProCA}$ is the dissociation constant between Gd^{3+} and ProCA32.collagen1, determined by eq 2.

The metal binding affinities were subsequently estimated as previously described.[11]

4.3.6. Transmetalation Studies. Transmetalation experiments of hProCA32.collagen in comparison with clinical contrast agents were done by obtaining the decrease in longitudinal relaxation rates of each contrast agent at 37 °C in phosphate buffer in the presence of Zn^{2+} over a period of 4 days. 50 μM hProCA32.collagen was incubated in a 1:2 hProCA32.collagen/metal ratio (100 μM Gd^{3+} and Zn^{2+}) in 1.2 mM PO_4^{3-}. The ratio of longitudinal relaxation at different time points over those observed at t = 0 were plotted against incubation time to obtain a plot depicting the rate of transmetalation[55]

4.3.7. Organ Toxicity Analysis of hProCA32.collagen by ICP. Healthy CD-1 mice were injected with 0.025 mmol/kg of hProCA32.collagen, and the mice were subsequently euthanized at

either 24 h or 14 days post-injection. Tissues from different organs of the mice were obtained, and approximately 0.2 g of the tissues was digested with 70% (w/v) grade ICP nitric acid (Fisher Chemical) in 37 °C water for 18−22 h. Undissolved contaminants were removed by filtration. The distribution of hProCA32.collagen in organs was obtained by analysis of the Gd^{3+} by inductively coupled plasma optical emission spectroscopy (ICP-OES). The Gd^{3+} content in each digested organ was measured by ICP-OES at wavelengths of 342 nm. The Gd^{3+} concentration was calibrated using different known concentrations of Gd^{3+} from 1 to 1000 ppb, and all experiments were done using 2 ppm of YCl_3 as internal reference.

4.3.8. Pharmacokinetic Studies and Acute Toxicity Studies. The tendency for hProCA32.collagen to cause acute toxicity to tissues was estimated as follows: Healthy 10-week-old CD-1 male and female mice (n = 9 per group) were intravenously injected with PBS as control and 7 mM hProCA32.collagen (0.035 mmol/kg). After the mice were euthanized at 48 h, various organs were harvested for organ size and toxicology analysis.

4.3.9. Lung SNR Estimation. All SNR values were analyzed using ImageJ software (https://imagej.nih.gov/ij/download.html). For all time points, regions of interest (ROIs) were drawn in the lung (signal), and in the background air next to the animal (noise). The ROIs were selected from all slices with full lung anatomy closely identical to the 0 h time point in each mice. First, the mice were compared at post-injection time points side-by-side with the pretime point to obtain slides with similarities. To calculate the time-dependent enhancement of hProCA32.collagen, the % change in enhancement was estimated by subtracting the baseline SNR from hProCA32.collagen-injected time points multiplied by 100.

The SNR values reported were calculated using

$$SNR = \frac{SI_{lung}}{SD_{background\ air}}$$

where SI_{lung} is the signal intensity of the lung and $SD_{background\ air}$ is the standard deviation of the background air.

4.3.10. AUC Analysis. To differentiate three stages (normal, early stage, late stage) of lung fibrosis, pattern changes were captured of lung SNR over 24 h (0, 1, 3, 24 h) in MRI images obtained from average T_1 values of 3D-UTE data. This was summarized as the AUC.

The percentage of SNR enhancement for each post-injection time-point was calculated as follows:

$$\% \text{ enhancement} = \left(\frac{\text{post-injection signal} - \text{pre-injection signal}}{\text{pre-injection signal}} \right) \times 100$$

SNR enhancement curves were plotted with code developed in R-studio to calculate the area under the curve (AUC_1−24). We used the 1 h data point as a reference instead of 0 h to calculate AUC_1−24h (area under the percentage of SNR enhancement curve in the time window of 1−24 h) to better differentiate the three stages. The enhancement and AUC calculation were repeated for each mouse from normal, early, and late-stage, and then AUC values among the three groups were compared with a two-tailed Student's t test (R studio). A P < 0.05 was considered significant.

4.3.11. Statistical Analysis. All experiments were performed using 4 to 6 mice in independent experiments. Details for each experiment are provided in the figure legends. Data analyses were performed using GraphPad Prism and R studio, with results presented as mean ± standard deviation or standard error of the mean. One-way ANOVA was used to compare normal and bleomycin or E-cigarette-treated mice. Student's t test compared data between normal and each diseased experimental group. P < 0.05 was considered statistically significant.

5. CONCLUSION

In the current work, we report that hProCA32.collagen-enabled collagen-targeted molecular MRI of IPF and COPD

with SNR values increasing with disease progression, and a linear correlation with histological characterization compared to nontargeted hProCA32 and clinically approved contrast agent Gadovist. hProCA32.collagen detected fibrotic changes in the lungs of IPF mice with a pattern similar to those observed with Sirius Red staining of the same mice, providing a novel noninvasive biomarker for progressive detection of IPF and COPD. We expect that further development of hProCA32.collagen-guided molecular MRI with an optimized imagining methodology to overcome motion artifacts, and optimized formulation and production, will further enhance the strong clinical translational potential for IPF and other lung diseases characterized by collagen overexpression.

■ ASSOCIATED CONTENT

Ⓢ Supporting Information

The Supporting Information is available free of charge at https://pubs.acs.org/doi/10.1021/cbmi.3c00023.

> Model structure and characterization of hProCA32.collagen, collagen binding specificity, relaxivity and metal binding plots of hProCA32.collagen, development of BM-treated IPF mice model, Arginase I staining, biodistribution, chemical and tissue toxicity test of hProCA32.collagen (PDF)

■ AUTHOR INFORMATION

Corresponding Author

Jenny J. Yang − *Department of Chemistry, Center for Diagnostics and Therapeutics, Advanced Translational Imaging Facility, Georgia State University, Atlanta, Georgia 30303, United States; InLighta Biosciences, Atlanta, Georgia 30303, United States;* ⓘ orcid.org/0000-0002-2310-7658; Phone: 404-413-5520; Email: jenny@gsu.edu; Fax: 404-413-5551

Authors

Oluwatosin Y. Ibhagui − *Department of Chemistry, Center for Diagnostics and Therapeutics, Advanced Translational Imaging Facility, Georgia State University, Atlanta, Georgia 30303, United States*

Dongjun Li − *Department of Chemistry, Center for Diagnostics and Therapeutics, Advanced Translational Imaging Facility, Georgia State University, Atlanta, Georgia 30303, United States*

Hongwei Han − *Department of Biology, Center for Diagnostics and Therapeutics, Georgia State University, Atlanta, Georgia 30303, United States*

Guangda Peng − *Department of Biology, Center for Diagnostics and Therapeutics, Georgia State University, Atlanta, Georgia 30303, United States*

Maureen L. Meister − *Department of Nutrition, Georgia State University, Atlanta, Georgia 30303, United States*

Zongxiang Gui − *Department of Chemistry, Center for Diagnostics and Therapeutics, Advanced Translational Imaging Facility, Georgia State University, Atlanta, Georgia 30303, United States*

Jingjuan Qiao − *Department of Chemistry, Center for Diagnostics and Therapeutics, Advanced Translational Imaging Facility, Georgia State University, Atlanta, Georgia 30303, United States; InLighta Biosciences, Atlanta, Georgia 30303, United States;* ⓘ orcid.org/0000-0002-4277-6531

Mani Salarian − *Department of Chemistry, Center for Diagnostics and Therapeutics, Advanced Translational Imaging Facility, Georgia State University, Atlanta, Georgia 30303, United States*

Bin Dong − *Department of Chemistry, Center for Diagnostics and Therapeutics, Advanced Translational Imaging Facility, Georgia State University, Atlanta, Georgia 30303, United States*

Yi Yuan − *Department of Biology, Center for Diagnostics and Therapeutics, Georgia State University, Atlanta, Georgia 30303, United States*

Yiting Xu − *Department of Chemistry, Center for Diagnostics and Therapeutics, Advanced Translational Imaging Facility, Georgia State University, Atlanta, Georgia 30303, United States*

Hua Yang − *Department of Ophthalmology, Emory University, Atlanta, Georgia 30322, United States*

Shanshan Tan − *Department of Chemistry, Center for Diagnostics and Therapeutics, Advanced Translational Imaging Facility, Georgia State University, Atlanta, Georgia 30303, United States*

Ganesh Satyanarayana − *Department of Biology, Center for Diagnostics and Therapeutics, Georgia State University, Atlanta, Georgia 30303, United States*

Shenghui Xue − *InLighta Biosciences, Atlanta, Georgia 30303, United States;* ⓘ orcid.org/0000-0001-8670-2131

Ravi Chakra Turaga − *Department of Biology, Center for Diagnostics and Therapeutics, Georgia State University, Atlanta, Georgia 30303, United States*

Malvika Sharma − *Department of Biology, Center for Diagnostics and Therapeutics, Georgia State University, Atlanta, Georgia 30303, United States*

Yan Hai − *Department of Statistics, Georgia State University, Atlanta, Georgia 30303, United States*

Yuguang Meng − *Department of Chemistry, Center for Diagnostics and Therapeutics, Advanced Translational Imaging Facility, Georgia State University, Atlanta, Georgia 30303, United States; Emory National Primate Research Center, Emory University, Atlanta, Georgia 30329, United States*

Khan Hekmatyar − *Department of Chemistry, Center for Diagnostics and Therapeutics, Advanced Translational Imaging Facility, Georgia State University, Atlanta, Georgia 30303, United States*

Phillip Sun − *Emory National Primate Research Center, Emory University, Atlanta, Georgia 30329, United States*

Gabriel Sica − *Winship Cancer Institute, Emory University, Atlanta, Georgia 30322, United States*

Xiangming Ji − *Department of Biology, Center for Diagnostics and Therapeutics, Georgia State University, Atlanta, Georgia 30303, United States;* ⓘ orcid.org/0000-0002-5941-0253

Zhi-ren Liu − *Department of Nutrition, Georgia State University, Atlanta, Georgia 30303, United States*

Complete contact information is available at:
https://pubs.acs.org/10.1021/cbmi.3c00023

Author Contributions

O.Y.I. and J.J.Y. designed the research and experiments and wrote the manuscript; G.P., H.H., G.S., O.Y.I., M.L.M., J.Q., X.J., and D.L. created animal models; O.Y.I., D.L., Z.G., B.D., Y.X., M.S., S.X., K.H., Y.X., and Y.M. analyzed the MRI data; R.C.T., G.S., H.Y., X.J., M. Sharma and Z.R.L. reviewed the

■ REFERENCES

(1) Quaderi, S. A.; Hurst, J. R. The unmet global burden of COPD. *Glob Health Epidemiol Genom* **2018**, *3*, e4.

(2) Richeldi, L.; Collard, H. R.; Jones, M. G. Idiopathic pulmonary fibrosis. *Lancet* **2017**, *389* (10082), 1941−1952.

(3) Totti, N., 3rd; McCusker, K. T.; Campbell, E. J.; Griffin, G. L.; Senior, R. M. Nicotine is chemotactic for neutrophils and enhances neutrophil responsiveness to chemotactic peptides. *Science* **1984**, *223* (4632), 169−171.

(4) Barnes, P. J. Small airway fibrosis in COPD. *Int. J. Biochem. Cell Biol.* **2019**, *116*, No. 105598.

(5) Vicary, G. W.; Ritzenthaler, J. D.; Panchabhai, T. S.; Torres-Gonzalez, E.; Roman, J. Nicotine stimulates collagen type I expression in lung via alpha7 nicotinic acetylcholine receptors. *Respir Res.* **2017**, *18* (1), 115.

(6) Raghu, G.; Remy-Jardin, M.; Myers, J. L.; Richeldi, L.; Ryerson, C. J.; Lederer, D. J.; Behr, J.; Cottin, V.; Danoff, S. K.; Morell, F.; Flaherty, K. R.; Wells, A.; Martinez, F. J.; Azuma, A.; Bice, T. J.; Bouros, D.; Brown, K. K.; Collard, H. R.; Duggal, A.; Galvin, L.; Inoue, Y.; Jenkins, R. G.; Johkoh, T.; Kazerooni, E. A.; Kitaichi, M.; Knight, S. L.; Mansour, G.; Nicholson, A. G.; Pipavath, S. N. J.; Buendia-Roldan, I.; Selman, M.; Travis, W. D.; Walsh, S.; Wilson, K. C.; American Thoracic Society, E. R. S. J. R. S.; Latin American Thoracic, S.. Diagnosis of Idiopathic Pulmonary Fibrosis. An Official ATS/ERS/JRS/ALAT Clinical Practice Guideline. *Am. J. Respir Crit Care Med.* **2018**, *198* (5), e44−e68.

(7) Tzilas, V.; Tzouvelekis, A.; Chrysikos, S.; Papiris, S.; Bouros, D. Diagnosis of Idiopathic Pulmonary Fibrosis "Pragmatic Challenges in Clinical Practice". *Front Med. (Lausanne)* **2017**, *4*, 151.

(8) Scelfo, C.; Caminati, A.; Harari, S. Recent advances in managing idiopathic pulmonary fibrosis. *F1000Res.* **2017**, *6*, 2052.

(9) Flaherty, K. R.; Travis, W. D.; Colby, T. V.; Toews, G. B.; Kazerooni, E. A.; Gross, B. H.; Jain, A.; Strawderman, R. L.; Flint, A.; Lynch, J. P.; Martinez, F. J. Histopathologic variability in usual and nonspecific interstitial pneumonias. *Am. J. Respir Crit Care Med.* **2001**, *164* (9), 1722−1727.

(10) Monaghan, H.; Wells, A. U.; Colby, T. V.; du Bois, R. M.; Hansell, D. M.; Nicholson, A. G. Prognostic implications of histologic patterns in multiple surgical lung biopsies from patients with idiopathic interstitial pneumonias. *Chest* **2004**, *125* (2), 522−526.

(11) Salarian, M.; Turaga, R. C.; Xue, S.; Nezafati, M.; Hekmatyar, K.; Qiao, J.; Zhang, Y.; Tan, S.; Ibhagui, O. Y.; Hai, Y.; Li, J.; Mukkavilli, R.; Sharma, M.; Mittal, P.; Min, X.; Keilholz, S.; Yu, L.; Qin, G.; Farris, A. B.; Liu, Z. R.; Yang, J. J. Early detection and staging of chronic liver diseases with a protein MRI contrast agent. *Nat. Commun.* **2019**, *10* (1), 4777.

(12) Xue, S.; Yang, H.; Qiao, J.; Pu, F.; Jiang, J.; Hubbard, K.; Hekmatyar, K.; Langley, J.; Salarian, M.; Long, R. C.; Bryant, R. G.; Hu, X. P.; Grossniklaus, H. E.; Liu, Z. R.; Yang, J. J. Protein MRI contrast agent with unprecedented metal selectivity and sensitivity for liver cancer imaging. *Proc. Natl. Acad. Sci. U. S. A.* **2015**, *112* (21), 6607−6612.

(13) Yang, J. J.; Yang, J.; Wei, L.; Zurkiya, O.; Yang, W.; Li, S.; Zou, J.; Zhou, Y.; Maniccia, A. L.; Mao, H.; Zhao, F.; Malchow, R.; Zhao, S.; Johnson, J.; Hu, X.; Krogstad, E.; Liu, Z. R. Rational design of protein-based MRI contrast agents. *J. Am. Chem. Soc.* **2008**, *130* (29), 9260−9267.

(14) Li, S.; Jiang, J.; Zou, J.; Qiao, J.; Xue, S.; Wei, L.; Long, R.; Wang, L.; Castiblanco, A.; White, N.; Ngo, J.; Mao, H.; Liu, Z. R.; Yang, J. J. PEGylation of protein-based MRI contrast agents improves relaxivities and biocompatibilities. *J. Inorg. Biochem.* **2012**, *107* (1), 111−118.

(15) Caravan, P.; Das, B.; Deng, Q.; Dumas, S.; Jacques, V.; Koerner, S. K.; Kolodziej, A.; Looby, R. J.; Sun, W. C.; Zhang, Z. A lysine walk to high relaxivity collagen-targeted MRI contrast agents. *Chem. Commun. (Camb)* **2009**, *4*, 430−432.

(16) Salarian, M.; Ibhagui, O.; Yang, J. Molecular Imaging of Extracellular Matrix Proteins with Targeted Probes using Magnetic Resonance Imaging. *WIREs Nanomedicine & Nanobiotechnology* **2020**, *12*, e1622.

(17) Caravan, P.; Yang, Y.; Zachariah, R.; Schmitt, A.; Mino-Kenudson, M.; Chen, H. H.; Sosnovik, D. E.; Dai, G.; Fuchs, B. C.; Lanuti, M. Molecular magnetic resonance imaging of pulmonary fibrosis in mice. *Am. J. Respir. Cell Mol. Biol.* **2013**, *49* (6), 1120−1126.

(18) Noebauer-Huhmann, I. M.; Szomolanyi, P.; Juras, V.; Kraff, O.; Ladd, M. E.; Trattnig, S. Gadolinium-based magnetic resonance contrast agents at 7 T: in vitro T1 relaxivities in human blood plasma. *Invest Radiol* **2010**, *45* (9), 554−558.

(19) Shen, Y.; Goerner, F. L.; Snyder, C.; Morelli, J. N.; Hao, D.; Hu, D.; Li, X.; Runge, V. M. T1 relaxivities of gadolinium-based magnetic resonance contrast agents in human whole blood at 1.5, 3, and 7 T. *Invest Radiol* **2015**, *50* (5), 330−338.

(20) Merbach, A. S.; Helm, L.; Merbach, A. E.; Tóth, E. ProQuest. *The Chemistry of Contrast Agents in Medical Magnetic Resonance Imaging*; John Wiley & Sons Inc., 2013.

(21) Hubner, R. H.; Gitter, W.; El Mokhtari, N. E.; Mathiak, M.; Both, M.; Bolte, H.; Freitag-Wolf, S.; Bewig, B. Standardized quantification of pulmonary fibrosis in histological samples. *Biotechniques* **2008**, *44* (4), 507−511.

(22) Han, H.; Peng, G.; Meister, M.; Yao, H.; Yang, J. J.; Zou, M. H.; Liu, Z. R.; Ji, X. Electronic Cigarette Exposure Enhances Lung Inflammatory and Fibrotic Responses in COPD Mice. *Front Pharmacol* **2021**, *12*, No. 726586.

(23) Travis, W. D.; Costabel, U.; Hansell, D. M.; King, T. E.; Lynch, D. A.; Nicholson, A. G.; Ryerson, C. J.; Ryu, J. H.; Selman, M.; Wells, A. U.; Behr, J.; Bouros, D.; Brown, K. K.; Colby, T. V.; Collard, H. R.; Cordeiro, C. R.; Cottin, V.; Crestani, B.; Drent, M.; Dudden, R. F.; Egan, J.; Flaherty, K.; Hogaboam, C.; Inoue, Y.; Johkoh, T.; Kim, D. S.; Kitaichi, M.; Loyd, J.; Martinez, F. J.; Myers, J.; Protzko, S.; Raghu,

G.; Richeldi, L.; Sverzellati, N.; Swigris, J.; Valeyre, D. An official American Thoracic Society/European Respiratory Society statement: Update of the international multidisciplinary classification of the idiopathic interstitial pneumonias. *Am. J. Respir Crit Care Med.* **2013**, *188* (6), 733−748.

(24) Richeldi, L.; du Bois, R. M.; Raghu, G.; Azuma, A.; Brown, K. K.; Costabel, U.; Cottin, V.; Flaherty, K. R.; Hansell, D. M.; Inoue, Y.; Kim, D. S.; Kolb, M.; Nicholson, A. G.; Noble, P. W.; Selman, M.; Taniguchi, H.; Brun, M.; Le Maulf, F.; Girard, M.; Stowasser, S.; Schlenker-Herceg, R.; Disse, B.; Collard, H. R. Efficacy and safety of nintedanib in idiopathic pulmonary fibrosis. *N Engl J. Med.* **2014**, *370* (22), 2071−2082.

(25) Margaritopoulos, G. A.; Vasarmidi, E.; Antoniou, K. M. Pirfenidone in the treatment of idiopathic pulmonary fibrosis: an evidence-based review of its place in therapy. *Core Evid* **2016**, *11*, 11−22.

(26) Galli, J. A.; Pandya, A.; Vega-Olivo, M.; Dass, C.; Zhao, H.; Criner, G. J. Pirfenidone and nintedanib for pulmonary fibrosis in clinical practice: Tolerability and adverse drug reactions. *Respirology* **2017**, *22* (6), 1171−1178.

(27) Spagnolo, P.; Kropski, J. A.; Jones, M. G.; Lee, J. S.; Rossi, G.; Karampitsakos, T.; Maher, T. M.; Tzouvelekis, A.; Ryerson, C. J. Idiopathic pulmonary fibrosis: Disease mechanisms and drug development. *Pharmacol Ther* **2021**, *222*, No. 107798.

(28) Richeldi, L.; Cottin, V.; Wurtemberger, G.; Kreuter, M.; Calvello, M.; Sgalla, G. Digital Lung Auscultation: Will Early Diagnosis of Fibrotic Interstitial Lung Disease Become a Reality? *Am. J. Respir Crit Care Med.* **2019**, *200* (2), 261−263.

(29) Montesi, S. B.; Izquierdo-Garcia, D.; Desogere, P.; Abston, E.; Liang, L. L.; Digumarthy, S.; Seethamraju, R.; Lanuti, M.; Caravan, P.; Catana, C. Type I Collagen-targeted Positron Emission Tomography Imaging in Idiopathic Pulmonary Fibrosis: First-in-Human Studies. *Am. J. Respir Crit Care Med.* **2019**, *200* (2), 258−261.

(30) Desogere, P.; Tapias, L. F.; Hariri, L. P.; Rotile, N. J.; Rietz, T. A.; Probst, C. K.; Blasi, F.; Day, H.; Mino-Kenudson, M.; Weinreb, P.; Violette, S. M.; Fuchs, B. C.; Tager, A. M.; Lanuti, M.; Caravan, P. Type I collagen-targeted PET probe for pulmonary fibrosis detection and staging in preclinical models. *Sci. Transl Med.* **2017**, *9* (384), eaaf4696.

(31) Akam, E. A.; Abston, E.; Rotile, N. J.; Slattery, H. R.; Zhou, I. Y.; Lanuti, M.; Caravan, P. Improving the reactivity of hydrazine-bearing MRI probes for in vivo imaging of lung fibrogenesis. *Chemical Science* **2020**, *11* (1), 224−231.

(32) Frenk, N. E.; Montesi, S. B.; Chen, T.; Liang, L. L.; Zhou, I.; Seethamraju, R.; Caravan, P.; Digumarthy, S. R. Free-breathing dynamic contrast-enhanced magnetic resonance of interstitial lung fibrosis. *Magn Reson Imaging* **2020**, *69*, 16−21.

(33) Schuster, D. P.; Kovacs, A.; Garbow, J.; Piwnica-Worms, D. Recent advances in imaging the lungs of intact small animals. *Am. J. Respir. Cell Mol. Biol.* **2004**, *30* (2), 129−138.

(34) Driehuys, B.; Walker, J.; Pollaro, J.; Cofer, G. P.; Mistry, N.; Schwartz, D.; Johnson, G. A. 3He MRI in mouse models of asthma. *Magn Reson Med.* **2007**, *58* (5), 893−900.

(35) Roos, J. E.; McAdams, H. P.; Kaushik, S. S.; Driehuys, B. Hyperpolarized Gas MR Imaging: Technique and Applications. *Magn Reson Imaging Clin N Am.* **2015**, *23* (2), 217−229.

(36) Svenningsen, S.; Eddy, R. L.; Lim, H. F.; Cox, P. G.; Nair, P.; Parraga, G. Sputum Eosinophilia and Magnetic Resonance Imaging Ventilation Heterogeneity in Severe Asthma. *Am. J. Respir Crit Care Med.* **2018**, *197* (7), 876−884.

(37) Farrar, C. T.; Gale, E. M.; Kennan, R.; Ramsay, I.; Masia, R.; Arora, G.; Looby, K.; Wei, L.; Kalpathy-Cramer, J.; Bunzel, M. M.; Zhang, C.; Zhu, Y.; Akiyama, T. E.; Klimas, M.; Pinto, S.; Diyabalanage, H.; Tanabe, K. K.; Humblet, V.; Fuchs, B. C.; Caravan, P. CM-101: Type I Collagen-targeted MR Imaging Probe for Detection of Liver Fibrosis. *Radiology* **2018**, *287* (2), 581−589.

(38) Waghorn, P. A.; Jones, C. M.; Rotile, N. J.; Koerner, S. K.; Ferreira, D. S.; Chen, H. H.; Probst, C. K.; Tager, A. M.; Caravan, P. Molecular Magnetic Resonance Imaging of Lung Fibrogenesis with an Oxyamine-Based Probe. *Angew. Chem., Int. Ed. Engl.* **2017**, *56* (33), 9825−9828.

(39) Wahsner, J.; Gale, E. M.; Rodriguez-Rodriguez, A.; Caravan, P. Chemistry of MRI Contrast Agents: Current Challenges and New Frontiers. *Chem. Rev.* **2019**, *119* (2), 957−1057.

(40) Akam, E. A.; Abston, E.; Rotile, N. J.; Slattery, H. R.; Zhou, I. Y.; Lanuti, M.; Caravan, P. Improving the reactivity of hydrazine-bearing MRI probes for in vivo imaging of lung fibrogenesis. *Chem. Sci.* **2020**, *11* (1), 224−231.

(41) Wahsner, J.; Desogere, P.; Abston, E.; Graham-O'Regan, K. A.; Wang, J.; Rotile, N. J.; Schirmer, M. D.; Santos Ferreira, D. D.; Sui, J.; Fuchs, B. C.; Lanuti, M.; Caravan, P. (68)Ga-NODAGA-Indole: An Allysine-Reactive Positron Emission Tomography Probe for Molecular Imaging of Pulmonary Fibrogenesis. *J. Am. Chem. Soc.* **2019**, *141* (14), 5593−5596.

(42) Mahmutovic Persson, I.; Falk Hakansson, H.; Orbom, A.; Liu, J.; von Wachenfeldt, K.; Olsson, L. E. Imaging Biomarkers and Pathobiological Profiling in a Rat Model of Drug-Induced Interstitial Lung Disease Induced by Bleomycin. *Front Physiol* **2020**, *11*, 584.

(43) Ersoy, H.; Rybicki, F. J. Biochemical safety profiles of gadolinium-based extracellular contrast agents and nephrogenic systemic fibrosis. *Journal of magnetic resonance imaging: JMRI* **2007**, *26* (5), 1190−1197.

(44) Montesi, S. B.; Rao, R.; Liang, L. L.; Goulart, H. E.; Sharma, A.; Digumarthy, S. R.; Shea, B. S.; Seethamraju, R. T.; Caravan, P.; Tager, A. M. Gadofosveset-enhanced lung magnetic resonance imaging to detect ongoing vascular leak in pulmonary fibrosis. *Eur. Respir. J.* **2018**, *51* (5), 1800171.

(45) Della Latta, V.; Cabiati, M.; Burchielli, S.; Frenzilli, G.; Bernardeschi, M.; Cecchettini, A.; Viglione, F.; Morales, M. A.; Del Ry, S. Lung inflammation after bleomycin treatment in mice: Selection of an accurate normalization strategy for gene expression analysis in an ex-vivo and in-vitro model. *Int. J. Biochem. Cell Biol.* **2017**, *88*, 145−154.

(46) Satyanarayana, G.; Turaga, R. C.; Sharma, M.; Wang, S.; Mishra, F.; Peng, G.; Deng, X.; Yang, J.; Liu, Z. R. Pyruvate kinase M2 regulates fibrosis development and progression by controlling glycine auxotrophy in myofibroblasts. *Theranostics* **2021**, *11* (19), 9331−9341.

(47) Han, H.; Zhang, Y.; Peng, G.; Li, L.; Yang, J.; Yuan, Y.; Xu, Y.; Liu, Z. R. Extracellular PKM2 facilitates organ-tissue fibrosis progression. *iScience* **2021**, *24* (10), No. 103165.

(48) Robson, M. D.; Gatehouse, P. D.; Bydder, M.; Bydder, G. M. Magnetic resonance: an introduction to ultrashort TE (UTE) imaging. *J. Comput. Assist Tomogr* **2003**, *27* (6), 825−846.

(49) Baues, M.; Dasgupta, A.; Ehling, J.; Prakash, J.; Boor, P.; Tacke, F.; Kiessling, F.; Lammers, T. Fibrosis imaging: Current concepts and future directions. *Adv. Drug Deliv Rev.* **2017**, *121*, 9−26.

(50) Haak, A. J.; Tan, Q.; Tschumperlin, D. J. Matrix biomechanics and dynamics in pulmonary fibrosis. *Matrix Biol.* **2018**, *73*, 64−76.

(51) Roach, D. J.; Cremillieux, Y.; Fleck, R. J.; Brody, A. S.; Serai, S. D.; Szczesniak, R. D.; Kerlakian, S.; Clancy, J. P.; Woods, J. C. Ultrashort Echo-Time Magnetic Resonance Imaging Is a Sensitive Method for the Evaluation of Early Cystic Fibrosis Lung Disease. *Ann. Am. Thorac Soc.* **2016**, *13* (11), 1923−1931.

(52) Togao, O.; Ohno, Y.; Dimitrov, I.; Hsia, C. C.; Takahashi, M. Ventilation/perfusion imaging of the lung using ultra-short echo time (UTE) MRI in an animal model of pulmonary embolism. *Journal of magnetic resonance imaging: JMRI* **2011**, *34* (3), 539−546.

(53) Sana, B.; Poh, C. L.; Lim, S. A manganese-ferritin nano-composite as an ultrasensitive T2 contrast agent. *Chem. Commun. (Camb)* **2012**, *48* (6), 862−864.

(54) Westbrook, C.; Talbot, J. *MRI in Practice*; Wiley-Blackwell, 2018.

(55) Laurent, S.; Vander Elst, L.; Copoix, F.; Muller, R. N. Stability of MRI paramagnetic contrast media: a proton relaxometric protocol for transmetallation assessment. *Invest Radiol* **2001**, *36* (2), 115−122.